land

MDPI

Article

Research on the Spatial-Temporal Evolution of Changsha's Surface Urban Heat Island from the Perspective of Local Climate Zones

Yanfen Xiang [1,2], Bohong Zheng [2], Jiren Wang [2], Jiajun Gong [2] and Jian Zheng [3,*]

[1] School of Landscape Architecture, Central South University of Forestry and Technology, Changsha 410004, China; 201301006@csu.edu.cn
[2] School of Architecture and Art, Central South University, Changsha 410075, China
[3] School of Architecture, Changsha University of Science and Technology, Changsha 410076, China
* Correspondence: zhengjian@csust.edu.cn

Abstract: Optimizing urban spatial morphology is one of the most effective methods for improving the urban thermal environment. Some studies have used the local climate zones (LCZ) classification system to examine the relationship between urban spatial morphology and Surface Urban Heat Islands (SUHIs). However, these studies often rely on single-time-point data, failing to consider the changes in urban space and the time-series LCZ mapping relationships. This study utilized remote sensing data from Landsat 5, 7, and 8–9 to retrieve land surface temperatures in Changsha from 2005 to 2020 using the Mono-Window Algorithm. The spatial-temporal evolution of the LCZ and the Surface Urban Heat Island Intensity (SUHII) was then examined and analyzed. This study aims to (1) propose a localized, long-time LCZ mapping method, (2) investigate the spatial-temporal relationship between the LCZ and the SUHII, and (3) develop a more convenient SUHI assessment method for urban planning and design. The results showed that the spatial-temporal evolution of the LCZ reflects the sequence of urban expansion. In terms of quantity, the number of built-type LCZs maintaining their original types is low, with each undergoing at least one type change. The open LCZs increased the most, followed by the sparse and the composite LCZs. Spatially, the LCZs experience reverse transitions due to urban expansion and quality improvements in central urban areas. Seasonal changes in the LCZ types and the SUHI vary, with differences not only among the LCZ types but also in building heights within the same type. The relative importance of the LCZ parameters also differs between seasons. The SUHI model constructed using Boosted Regression Trees (BRT) demonstrated high predictive accuracy, with R^2 values of 0.911 for summer and 0.777 for winter. In practical case validation, the model explained 97.86% of the data for summer and 96.77% for winter. This study provides evidence-based planning recommendations to mitigate urban heat and create a comfortable built environment.

Keywords: local climate zones (LCZ); surface urban heat island intensity (SUHII); spatial-temporal evolution; long-time LCZ mapping; Boosted Regression Trees (BRT)

check for updates

Citation: Xiang, Y.; Zheng, B.; Wang, J.; Gong, J.; Zheng, J. Research on the Spatial-Temporal Evolution of Changsha's Surface Urban Heat Island from the Perspective of Local Climate Zones. *Land* **2024**, *13*, 1479. https://doi.org/10.3390/land13091479

Academic Editor: Thomas Panagopoulos

Received: 5 August 2024
Revised: 9 September 2024
Accepted: 11 September 2024
Published: 12 September 2024

Copyright: © 2024 by the authors. Licensee MDPI, Basel, Switzerland. This article is an open access article distributed under the terms and conditions of the Creative Commons Attribution (CC BY) license (https://creativecommons.org/licenses/by/4.0/).

1. Introduction

Global warming is widely regarded as the foremost threat humanity faces in the 21st century, posing significant challenges to sustainable development. Human activities have already caused approximately a 1.0 °C increase in global temperatures compared to pre-industrial levels [1]. As the largest developing country, China's warming trend aligns with the global pattern, with a rate of increase surpassing the global average [2]. From 1951 to 2021, China's annual average surface temperature rose significantly at a rate of 0.26 °C per decade, notably higher than the global and Northern Hemisphere averages. The built-up areas of 75 major Chinese cities expanded 7.46 times from 1972 to 2020 [3], drastically altering urban surfaces. The replacement of natural surfaces with impermeable materials

like concrete and asphalt has escalated urban temperatures and intensified the urban heat island (UHI) effect [4]. Thus, mitigating the UHI effect is crucial for the sustainable development of Chinese cities.

The intensity of the Surface Urban Heat Islands (SUHIs) has garnered significant attention in analyzing the UHI effect. UHI refers to the phenomenon where urban areas are warmer than their rural surroundings, typically assessed using air temperature (AT) [5,6] or land surface temperature (LST) [7,8]. AT is measured at pedestrian height within the urban canopy, usually via fixed weather stations or mobile sensors [9]. LST, the temperature of the ground surface influenced by solar radiation and long-wave radiation, is commonly obtained through remote sensing. AT data allows for long-term series studies due to its extended observation periods. However, it has limitations, including the limited distribution of urban weather stations, low spatial resolution, significant scale effects, and high costs in terms of data collection and manpower [10]. In contrast, LST data offer extensive coverage, high spatial resolution, and real-time large-area observations, effectively reflecting urban expansion. Consequently, LST is selected as the focus of this study.

The Local Climate Zones (LCZs) classification system effectively addresses the heterogeneity and spatial autocorrelation of urban areas. The LCZs evolved from urban climate maps and various classification schemes [11] and abstractly represent complex surface forms with temperature-sensitive indicators based on extensive field surveys. The LCZ classification methods include remote sensing, ArcGIS-based, and combined mapping approaches. Remote sensing methods, such as those used in the WUDAPT project, are essentially based on the LCZ classification of remote sensing image data, but they often lack precision [12,13]. ArcGIS-based methods, which rely on urban datasets of GIS vector format land and building data, achieve higher accuracy but face challenges in acquiring complete GIS data [14,15]. The combined mapping approach integrates the strengths of both methods [16–18], making it ideal for creating LCZ maps. However, time-series LCZ data are crucial for the temporal analysis of UHI and other urban climate studies, especially in rapidly urbanizing developing countries [19]. Previous studies typically used single-time-point data, limiting applicability and assuming changes in building types and landscapes [20,21]. This means that transformations from built-up areas to natural landscapes or from high-rise buildings to low-rise buildings seldom occur [19]. Additionally, few LCZ mapping methods in previous studies took account of the temporal consistency of the LCZs between different years [19,22]. Ensuring temporal consistency in the LCZs is necessary for accurate urban planning and strategy formulation in China's fast-urbanizing cities.

The LCZ scheme's detailed classification of urban spaces facilitates the UHI research. Previous studies often calculated the Surface Urban Heat Islands Intensity (SUHII) as the LST difference between urban and rural areas, while definitions of "urban" and "rural" sites vary across different study areas, and the simple one urban category homogenizes intra-urban difference of heat island. Some researchers have combined the LCZ scheme with LST to explore LST/SUHI variations in different cities, like Prague and Brno in the Czech Republic [23], West Bengal in India [24], Nanjing in China [25], and Fuzhou in China [26]. Studies to date suggest that the use of LST has shown a reasonable ability to discriminate between the LCZ classes. However, the thermal characteristics of urban functional areas differ significantly [27]. Stewart and Oke [11] proposed a new UHI framework based on the LCZ temperature differences rather than "urban–rural" differences, considering the three-dimensional morphological and structural differences between urban and rural areas, thus providing a scientific evaluation of the UHI.

Exploring the impact of urban space on the UHI through surface parameters has been widely applied. Early researchers used climate models like ENVI-met [28] and PHOENICS [29] to study urban climate changes and UHI assessment [30], but numerical simulations require a longer time. The use of GIS and remote sensing technologies has not only provided detailed scale data on buildings and LST but has also greatly saved time and offered alternative methods for studying the impact of urban morphology on thermal

environments [31–33]. Extensive research indicates a non-linear relationship between urban morphology and LST/SUHI, with non-linear models outperforming linear ones [34]. Various machine learning models, such as Random Forests [26,35], Boosted Regression Trees (BRT) [33,36,37], Artificial Neural Networks [38], and extreme gradient boosting (XGBoost) [39], have been used to study urban morphology's impact on LST/UHI. Among these, BRT, combining the strengths of boosting and regression trees, is widely used in ecological and environmental studies [40] for its robust non-linear relationship capture and identifying the relative importance of influencing factors. Notably, it is highly robust against multicollinearity, making it a promising tool for constructing LST predictive models [41].

This study employs LCZ mapping to detect the spatial-temporal variations of the SUHI and relate it to the SUHI variation in Changsha city. By analyzing data from 2005 to 2020, a localized LCZ classification system for Changsha has been constructed, generating multi-time series LCZ maps and analyzing the quantitative changes and spatial distribution. The distribution of the SUHI from 2005 to 2020 has been analyzed to identify trends in land cover changes and the SUHI variations across different years. Additionally, differences in the SUHII within each LCZ type have been explored. Lastly, the BRT model has been utilized to construct a predictive model for spatial morphology indicators and SUHI. These findings aim to provide scientific strategies for urban planners and administrators to optimize urban landscapes and building designs, mitigating the SUHI increases in built-up areas from an LCZ perspective.

2. Data and Methods

2.1. Study Area

Changsha (111.54′–114.15′ E, 27.51′–28.40′ N) is the capital of Hunan Province and the central city of the Greater Changsha Metropolitan Region (Figure 1). Located in central China, this city has undergone significant urban development. By the end of 2022, the urbanization rate had reached 83.27%. With a total resident population of 10.42 million, it became the city with the largest population growth in the country [42]. Changsha boasts a diverse and vastly varying terrain, spanning elevations from 21.6 to 1607.9 m, complemented by a robust surface water system. The city can be classified as the Warm Temperate Moist Climate (Cfa) type in the Köppen–Geiger Climate Zone [43], characterized by distinct seasons and a significant monsoon influence, resulting in ample rainfall that coincides with heat. Extreme temperatures can reach as high as 43.0 °C in the summer and as low as −5.0 °C in the winter [10], earning it the reputation of a city with sweltering summers and chilly winters. Renowned as a "furnace" city, Changsha recorded an impressive 395 high-temperature days from 2010 to 2021, averaging 32.9 days annually, with intense heatwaves frequently intensifying in July and August [44]. Therefore, this city is an ideal subject for studying the urban heat island effect. The focus of this research is on the main area of Changsha, enclosed by the third ring road, covering approximately 680.06 km^2 (Figure 1).

2.2. Data

The study obtained the Landsat 5, Landsat 7, and Landsat 8–9 remote sensing data from the USGS Earth Explorer website (https://earthexplorer.usgs.gov/, accessed on 8 August 2023) to calculate LST. Collected remote sensing images from July to August in summer and December in winter, with cloud cover below 10. The specific parameters are shown in Table 1. Many researchers use the MODIS remote sensing data for research [45,46]. Although the MODIS remote sensing has a high temporal resolution (4 times a day), its low spatial resolution is 1000 m, which is unsuitable for studying fine-grained heterogeneous urban space, and there are significant errors in inverting the LST within the city. In contrast, the spatial resolution of Landsat series remote sensing data is 30 m, which has a higher spatial resolution than the MODIS. Due to the 2015 data not meeting the filtering criteria, remote-sensing images from 2016 were selected.

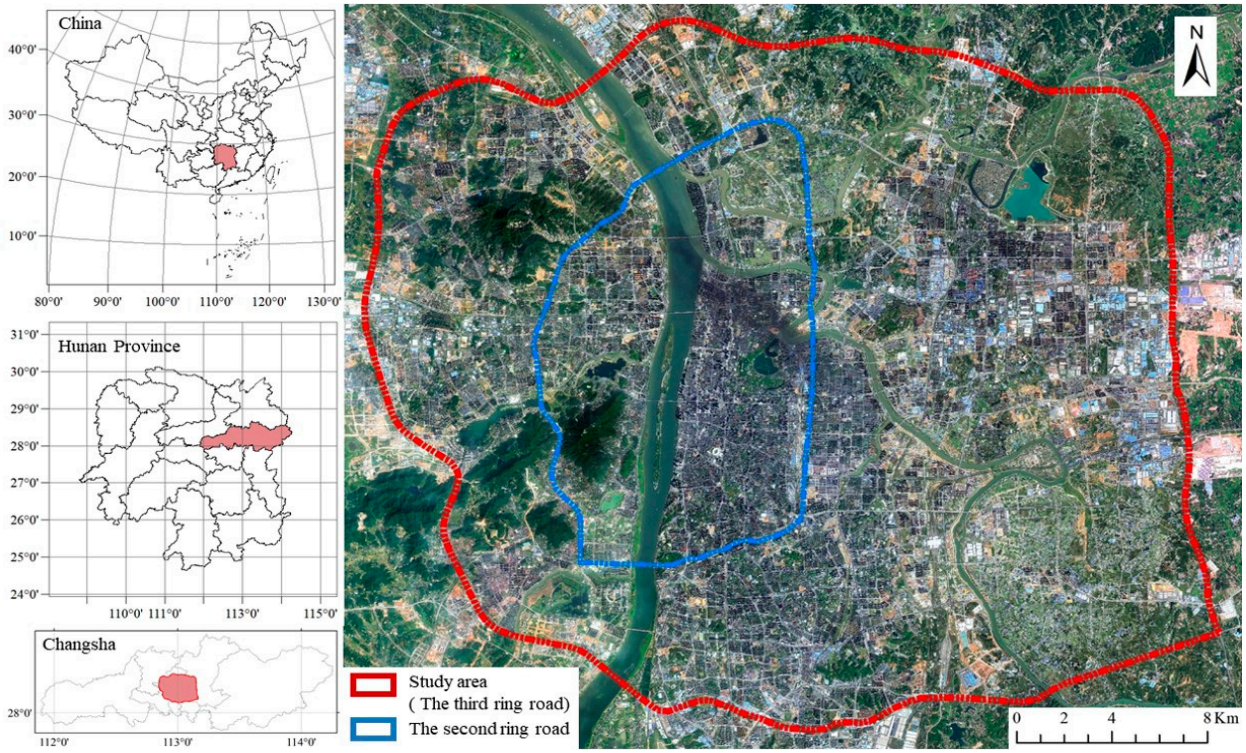


Figure 1. The location of the study area.

Table 1. The dates and related parameters of remote sensing images.

Year	Satellite Model	Season	Data (m/d)	WRS Path/Row	Sun-Elevation	Sun-Azimuth	Land Cloud Cover
2005	Landsat 7	Summer	8/2	123/40	63.15357870	108.55007428	4.00
			8/2	123/41	63.35264972	105.55576563	3.00
		Winter	12/8	123/40	33.84027840	154.27640755	0.00
			12/8	123/41	35.02755534	153.57313566	0.00
2010	Landsat 5	Summer	8/21	123/40	60.68345466	119.52856771	4.00
			8/21	123/41	61.15568514	116.93293115	2.00
	Landsat 7	Winter	12/22	123/40	32.94643872	153.95202880	0.00
			12/22	123/41	34.13052128	153.26324036	1.00
2016	Landsat 8–9	Summer	7/23	123/40	66.49031153	106.76246786	1.63
			7/23	123/41	66.63615756	103.29242434	3.11
		Winter	12/30	123/40	33.48688786	154.53316225	3.94
			12/30	123/41	34.67955246	153.84089683	0.15
2020	Landsat 8–9	Summer	8/3	123/40	65.27432146	112.38536985	5.61
			8/3	123/41	65.56427737	109.13729274	8.04
		Winter	12/25	123/40	33.50019512	155.29162805	0.22
			12/25	123/41	34.70360411	154.60980959	0.44

2.3. Methods

2.3.1. LCZ Mapping

LCZ Parameters

The LCZ encompasses both geometric attributes and surface cover characteristics, with its parameters meticulously categorized into two-dimensional (2D) land cover indicators and three-dimensional (3D) building form indicators. The land cover indicators encompass Pervious Surface Fraction (PSF), Impervious Surface Fraction (ISF), Albedo (AL), Terrain Roughness Class (Z_0), and Normalized Difference Vegetation Index (NDVI), while the building form indicators comprise Sky View Factor (SVF), Building Height ($\overline{BH}$), Height

Standard Deviation (HSD), Building Surface Fraction (BSF), and Floor Area Ratio (FAR). Notably, the land cover indicators are derived from remote sensing data [47,48], whereas the building form indicators stem from census data. Table 2 provides a comprehensive overview of each indicator's detailed description.

Table 2. The LCZ parameters selected in this study.

Parameter		Description	Formula
2D	PSF [26]	Proportional pervious surface area of a grid.	$PSF = PSA/A_{\mathrm{i}}$ where PSA is the pervious surface area, and A_i is the grid area of grid number i.
	ISF [26]	Proportional impervious surface area of a grid.	$ISF = ISA/A_{\mathrm{i}}$ where ISA is impervious surface area, and A_i is the grid area of grid number i.
	AL [49]	Represents the heat balance on the Earth's surface.	$\alpha_{short} = \frac{0.356\rho_1+0.130\rho_3+0.373\rho_4+0.085\rho_5+0.072\rho_7-0.0018}{0.356+0.130+0.373+0.085+0.072}$ where ρ represents Landsat bands 1, 3, 4, 5 and 7.
	Z_0 [50]	Roughness length describing the terrain surface (building geometry and land cover).	The roughness length is classified according to the classification system proposed by Davenport et al.
	NDVI [51]	It is effective for expressing vegetation status and quantified vegetation attributes.	$NDVI = \frac{NIR-Red}{NIR+Red}$ where Red and NIR are spectral radiance (or reflectance) measurements recorded with sensors in red (visible) and NIR regions, respectively.
3D	SVF [52,53]	The fraction of the overlying hemisphere occupied by the sky.	$\psi_{SVF} = 1 - i\sum \sin^2 \beta_i \left(\frac{\alpha_i}{360^\circ}\right)$ where α_i is the azimuth angle, and β_i is the maximum tilt angle along the pixel direction of the obstruction.
	$\overline{\mathrm{BH}}$	The weighted average height of buildings in the grid.	$\overline{BH} = \sum_{i=1}^{n} H_i W_i$ where i is the building number, n is the total number of buildings in the grid, H is the building height, and W_i is the weight value of the total building area of building number i in the grid area.
	HSD [26]	Variation degree of the building height of a grid.	$HSD = \sqrt{\frac{\sum_{i=1}^{n}\left(H_i-\overline{H}\right)^2}{n-1}}$ where i is the building number, n is the total number of buildings in the grid, H is the building height and $\overline{H}$ is the average building height.
	BSF [32]	The ratio of the footprint area of buildings to the total area of the grid.	$BSF = \sum_{i=1}^{n} A_{arc}/A_j$ where i is the building number, A_{arc} is the footprint area of the i building, j is the grid number, and A_j is the grid area of grid number j.
	FAR [54]	The ratio of the floor area of the buildings to the total area of the grid.	$FAR = \sum_{i=1}^{n} A_{arc}F/A_j$ where i is the building number, A_{arc} is the footprint area of the i building, F is the number of floors of building number i, j is the grid number, and A_j is the grid area of grid number j.

Classification Procedure

The classification of the LCZ can be divided into three methods: Remote Sensing (RS)-based, GIS-based, and a combination of both. Extensive research has been conducted on the selection of these methods [17,55]. Each of the first two methods has its advantages and disadvantages, while the combined approach leverages the strengths of both. In this study, we used the combined method: RS for identifying land cover types in the LCZ and GIS for classifying building types within the LCZ. The classification was executed using Python 3.12 scripts on the ArcGIS 10.8 platform [20]. Firstly, the morphology data and land cover data were processed in the GIS platform, and a database was established. Secondly, the datasets were processed according to the calculation formula in Table 2 to obtain the LCZ parameter. Thirdly, the LCZ grid was constructed, and the datasets were superimposed. Finally, the LCZ types of each grid were classified according to the LCZ parameter.

LCZ Raster

The optimal spatial resolution for the LCZ determination is based on scale effect analysis. According to Oke [56], the minimum diameter for each LCZ should be 400–1000 m. Studies by Thomas and Grégoire [57], Rodler and Leduc [58], and Zheng et al. [59] indicate that the optimal spatial resolution for the LCZ varies between cities due to differences in building geometry. The semivariogram function can be used to determine the appropriate LCZ diameter range for the study area. In this research, we applied the ordinary kriging model for semivariogram analysis, a geostatistical method used for spatial modeling and structure analysis. The formula is as follows:

$$Semivariogram(h) = 0.5 \times \sum \left[(Z(x) - Z(x+h))^2 \right] / N(h) \quad (1)$$

where $Semivariogram(h)$ represents the semivariogram value depending on the distance h between two sample points, $Z(x)$ denotes the measurement at position x, $Z(x + h)$ represents the measurement at distance h from position x, and $N(h)$ is the number of sample pairs within distance h.

LCZ Types Transition

To monitor the development of LCZ types in the region, a change detection analysis based on land cover transformation matrices was conducted. This analysis highlights the transitions between different LCZ types over specific periods. The matrix provides precise areas of each LCZ at distinct time points and indicates the extent of area transferred from one LCZ type to another from the beginning to the end of the study period. These transformation data are effectively captured by the matrix [60].

$$S_{ij} = \begin{bmatrix} S_{11} & S_{12} & \cdots & S_{1G} \\ S_{21} & S_{22} & \cdots & S_{2G} \\ \vdots & \vdots & \vdots & \vdots \\ S_{G1} & S_{G2} & \cdots & S_{GG} \end{bmatrix} \quad (2)$$

where i represents the LCZ type area in the initial period (i = 1, 2,. . ., 6, 8, 11, 91, 92, 93, 91E, 92E, 93E, A, C, E, EA, F, G), j represents the LCZ type area in the subsequent period (j = 1, 2,. . ., 6, 8, 11, 91, 92, 93, 91E, 92E, 93E, A, C, E, EA, F, G), and S_{ij} is the area transferred between different LCZ types.

LST Inversion

Currently, there are mainly three types of surface temperature retrieval algorithms, the Radiative Transfer Equation, the Mono-Window Algorithm, and the Split-Window Algorithm [61]. Xiang et al. [10] have used these algorithms for surface temperature inversion in Changsha city. Compared with the Radiative Transfer Equation and the Split-Window Algorithm, the Mono-Window Algorithm exhibits greater sensitivity and broader applicability [62,63]. Landsat remote sensing images are used in the radiative transfer, mainly including the following processes: radiation calibration, atmospheric correction, image mosaic, NDVI calculation, vegetation coverage calculation, TIRS band 10 brightness temperature calculation, land surface emissivity calculation, blackbody radiance calculation (at the same temperature), and LST calculation. The formula for the Mono-Window Algorithm is as follows:

$$T_s = [\mathrm{a}(1 - C - D) + (b(2 - C - D) + C + D)T_{sensor} - DT_a]/C \quad (3)$$

where T_s is the LST retrieved from the Landsat 8 TIRS Band 10 data; T_a is the effective mean atmospheric temperature; T_{sensor} is the brightness temperature of Landsat 8–9 TIRS Band 10; a and b are the coefficients used to approximate the derivative of the Planck radiance

function for the TIRS Band 10, $a = -67.355351$, $b = 0.458606$; and C and D are the internal parameters for the algorithm based on the atmospheric parameters and ground emissivity.

Surface Urban Heat Island Intensity Calculation

The calculation of urban heat island intensity has been expressed differently in different studies. Stewart and Oke [11] suggested using the LCZ-D as a calculation benchmark in the theory of local climate zones to study the relative differences between different built types and the LCZ-D. However, our analysis of current surface temperature data revealed that the coolest form in vegetation types is the LCZ-A, not the LCZ-D. Additionally, the base data in this study could not distinguish between shrubs and low vegetation, thus merging them into the LCZ-C. Consequently, this study uses the surface temperatures of the LCZ-A and LCZ-C as the baseline. The SUHI is defined as the difference in surface temperature between any LCZ type and the LCZ-A+C, calculated as follows:

$$SUHII = LST_{LCZ\text{-}X} - LST_{LCZ\text{-}A+C} \quad (4)$$

where the $LST_{LCZ\text{-}X}$ denotes the surface temperature values of various LCZ types, and the $LST_{LCZ\text{-}A+C}$ represents the average surface temperature of the LCZ-A and LCZ-C.

Relevant Models

The Boosted Regression Trees (BRT) model, a machine learning algorithm developed by Elith et al. [64], is based on classification and regression trees and is used to fit statistical models. It effectively explains and predicts non-linear relationships between variables. Initially used in ecological studies, BRT is now applied to understand how urban spatial characteristics influence LST. The BRT model combines weak learners and strong predictive rules, allowing flexible feature space partitioning. Unlike traditional regression models, BRT captures non-linear relationships between independent and predictor variables by combining regression trees and boosting algorithms.

The construction of the BRT model requires setting core parameters: Learning Rate (LR), Tree Complexity (TC), Number of Trees (NT), and Bagging Fraction (BF) [32,35]. In this study, parameter combinations were tested to achieve regularization, with the final combination being LR = 0.005, TC = 5, and BF = 0.5. We used 70% of the data as the training set and selected the optimal model using 10-fold cross-validation. The model implementation was performed using the "gbm", "rgdal", and "brt" packages in R.

Polynomial regression is a mathematical model that represents the relationship between variables as a polynomial, which is an algebraic expression composed of several monomials. Non-linear regression models achieve better fits to complex data patterns by adding polynomial terms or higher-degree terms (such as squares and cubes of predictor variables).

Spline regression can be seen as piecewise or segmented regression. It divides the dataset into multiple continuous intervals, with the division points called knots. Each interval is fitted with a separate model, making the model more flexible as the number of knots increases. While polynomial regression provides a global explanation of the dataset, spline regression offers a local explanation. Generally, spline regression yields better outputs than polynomial regression due to its localized approach.

Estimation Indicators

A series of statistical evaluation indicators, including R-squared (R^2), R-squared SD (R^2 SD), Root Mean Squared Error (RMSE), and Mean Absolute Error (MAE), were selected to quantify the accuracy of the original and revised diagnostic equation model. R^2 represents model accuracy and predictive ability, R^2 SD measures the uncertainty of model fit, RMSE compares the average error between predicted and observed results, and MAE accurately reflects the size of the actual prediction error. The indicators were quantified based on the following equations:

$$R^2 = 1 - SS_{\text{res}} / SS_{tot} \quad (5)$$

where SS_{res} (Residual Sum of Squares) is the sum of the squares of the differences between the observed and predicted values, and SS_{tot} (Total Sum of Squares) is the sum of the squares of the differences between the observed values and the mean of the observed values.

$$RMSE = \sqrt{\frac{\sum_{i=1}^{n} (X_{measure,i} - X_{\mathrm{model},i})^2}{n}} \quad (6)$$

$$MAE = \mathrm{n}^{-1} \sum_{i=1}^{n} \left| X_{measure,i} - X_{\mathrm{model},i} \right| \quad (7)$$

where $X_{measure}$ represents the temperature value of the observation point, X_{model} represents the model predicted temperature, and n represents the number of observation points.

3. Results

3.1. Construction of the LCZ Classification System for Changsha

3.1.1. Spatial-Temporal Distribution of the LCZ Parameters

The spatial-temporal distribution of the LCZ parameters (Figure 2) reveals significant variations over time. In the land cover parameter (2D), the total area of PSF has decreased while the ISF has increased. Notably, cropland and forest areas in the PSF have reduced by 25.70% and 6.96%, respectively, especially near the central urban area (Table A5). The ISF expanded from 27.86% to 57.06%, radiating outward in a star-shaped pattern consistent with urban expansion. With the reduction in the PSF, the area of NDVI is also affected, and overall, showing higher coverage and abundance in summer than in winter. The AL varied significantly between seasons, with higher vegetation abundance and shorter light path length in summer leading to greater solar absorption, reducing surface reflectance. However, whether in summer or winter, the high AL value is concentrated in industrial parks and railway hubs, with farmland exhibiting higher AL than built-up areas. The difference is that the value is higher in summer, and the AL value of water bodies is lower. Over time, urban space types diversified, and the Z_0 showed an increase in rough, very rough, and chaotic types scattered throughout the urban area.

The building morphology parameters (3D) also changed significantly in spatial layout and quantity. Low-rise and multi-story industrial buildings gradually moved to the periphery, while high-rise residential and skyscraper complexes increased, shifting from a centralized core development to a multi-centric pattern. The tallest building in 2020 reached 452 m (Changsha IFS). The increased concentration of skyscrapers in the central urban area led to greater height variation within the region. Proper building density is essential for creating comfortable urban spaces; excessive or insufficient density can cause spatial oppression or land wastage. In the study area, 96% of the BSF ranged from 0 to 0.4, indicating a reasonable distribution. High values appeared in areas with large factory buildings (such as Lugu High-Tech Industrial Park) and high-density historic districts (like Taiping Street). The FAR increased over time, especially with the rise in skyscrapers, reaching a maximum of 11.37 (Changsha IFS), while low values were mostly in suburban areas. The SVF decreased as vertical urban spaces developed, particularly in the central area, with lower values in suburban natural surfaces and low-rise industrial parks.

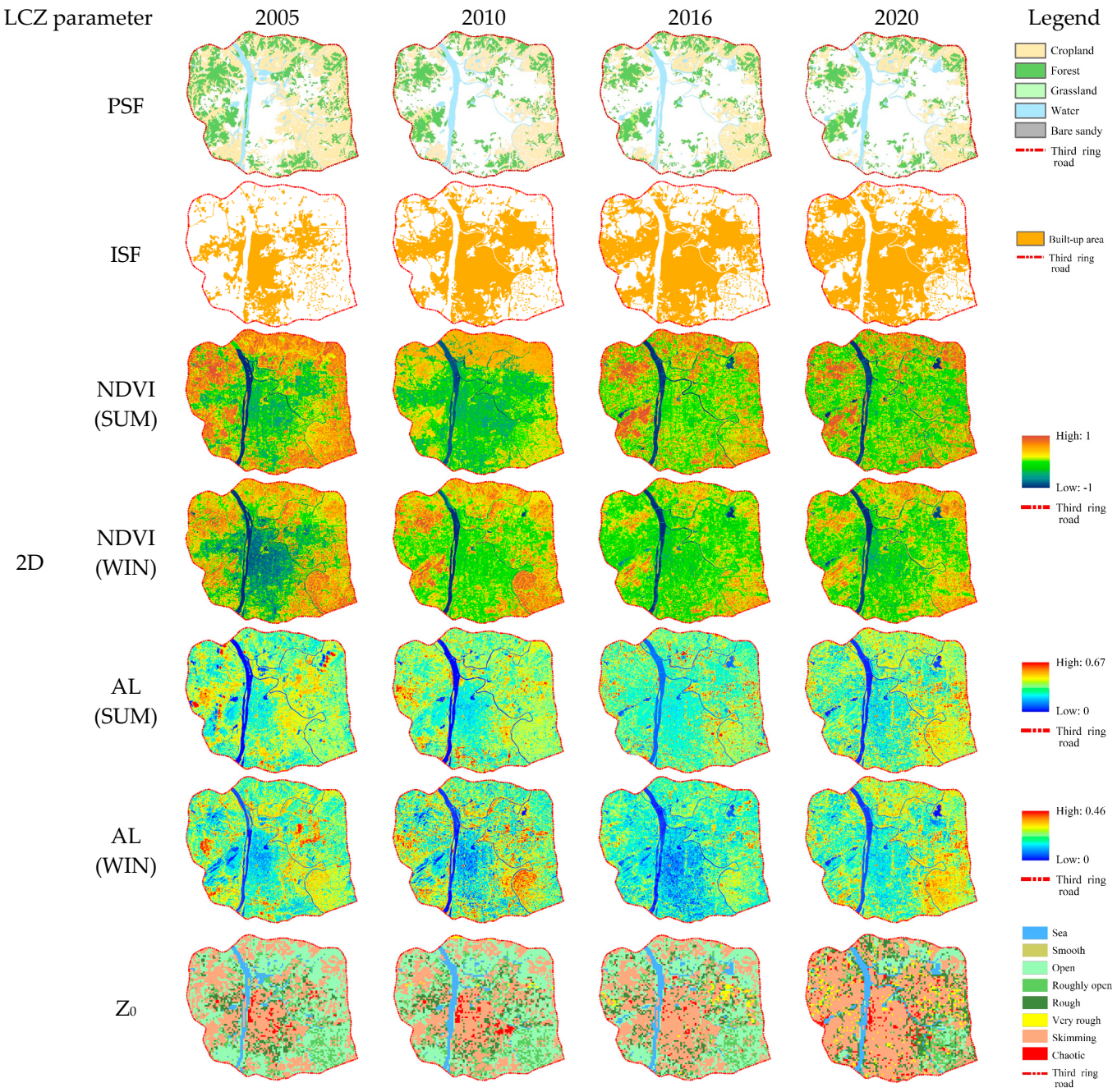


Figure 2. *Cont.*

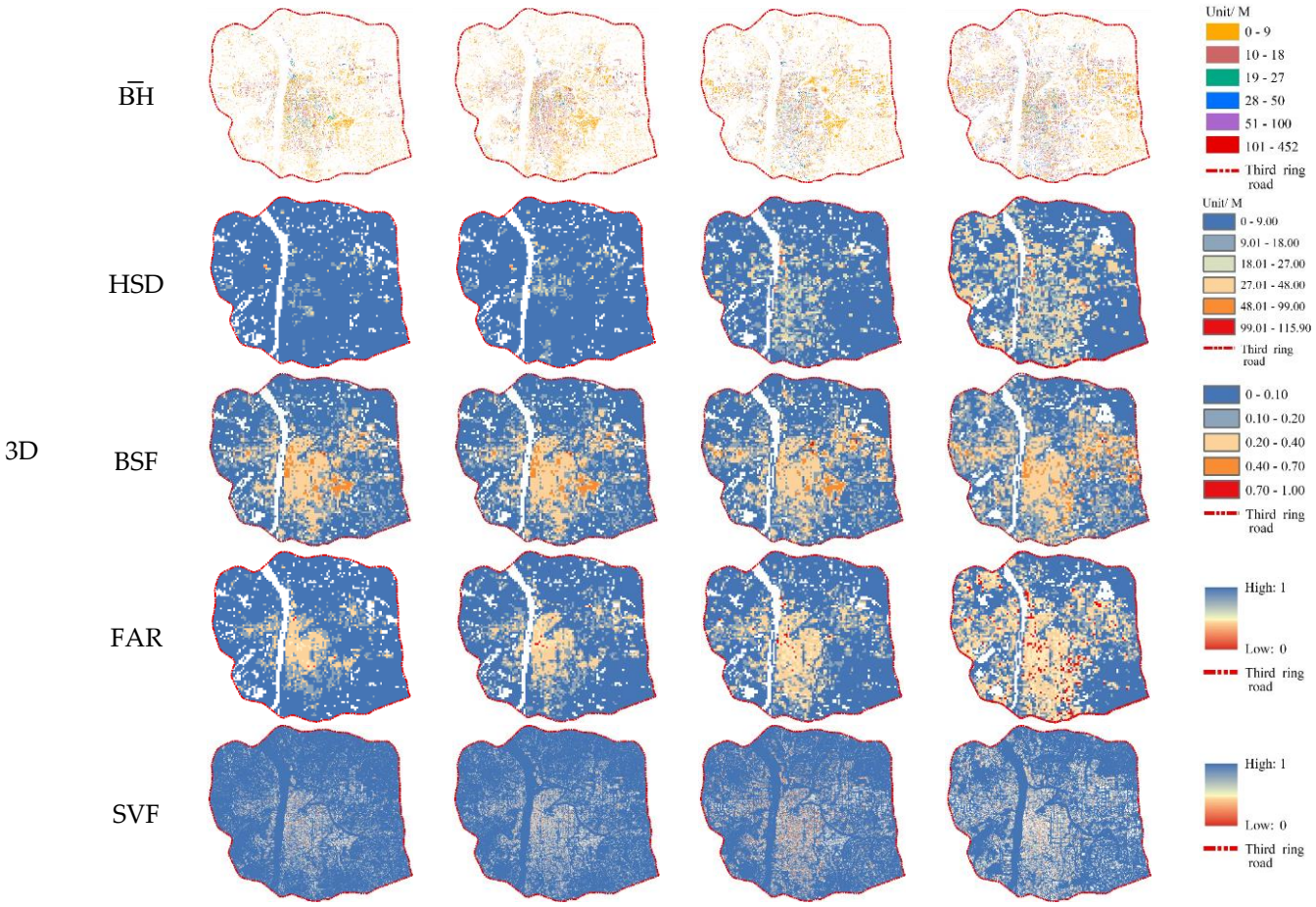


Figure 2. Distribution of LCZ Parameters from 2005 to 2020.

3.1.2. Determining the LCZ Grid Size

Spatial resolution, exhibiting heterogeneity and scale dependency, significantly impacts the research process and results. Low-resolution observations might appear homogeneous, whereas high-resolution studies could reveal non-uniformity, increasing the complexity of analysis due to redundant information and vast data. Thus, determining the optimal spatial resolution for the LCZ is crucial. The semivariogram of building height from 2005 to 2020 (Figure 3) shows increased semi-variance with distance, peaking at approximately 300 m. The red dots represent binned values, grouped from empirical semivariogram points, with the mean values shown as blue crosses. Comparison across years indicates stability around the 300 m mark, suggesting strong autocorrelation within this range. Therefore, a 300 m grid size was chosen, encompassing 7674 grid units in the study area.

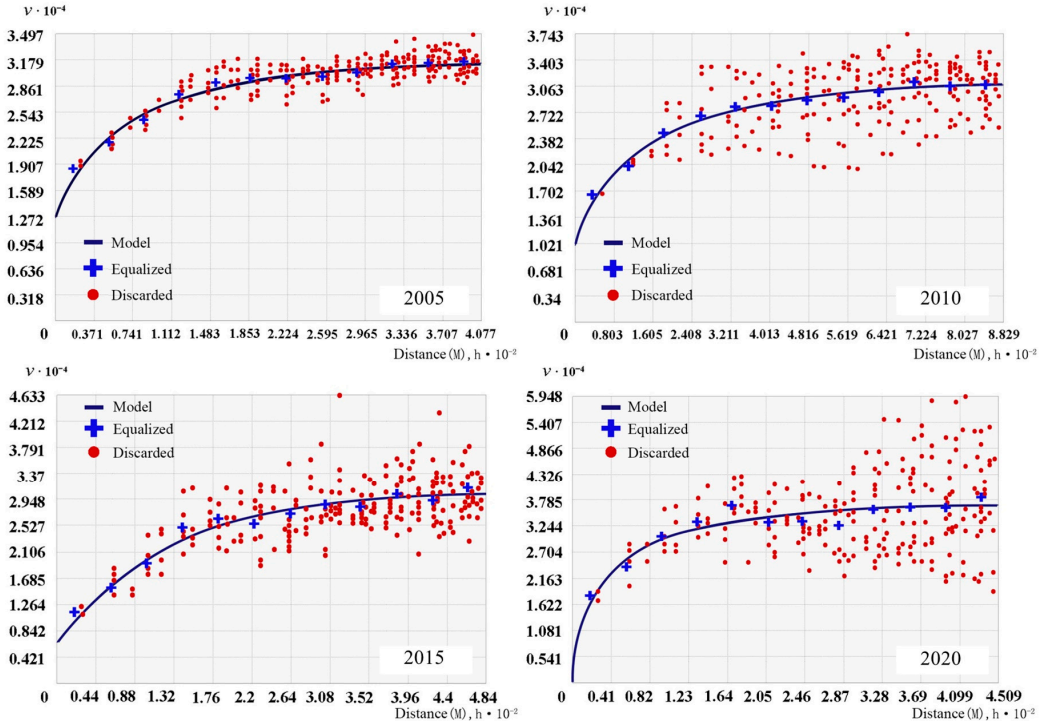


Figure 3. The semivariogram model of building height.

3.1.3. Classification System

The LCZ types for Changsha were adjusted based on local surveys. Some indicators in the original standard set were either not covered or included, necessitating adjustments. The revised system comprises 20 types: 6 land cove types and 14 built types (Figure 4). The LCZ-9 was subdivided into the sparse high-rise (LCZ-91), midrise (LCZ-92), low-rise (LCZ-93), and the composite high-rise (LCZ-91E), midrise (LCZ-92E), and low-rise (LCZ-93E). New categories of the low-density high-rise (LCZ-11) and the half-bare rock and half trees (LCZ-EA) were added.

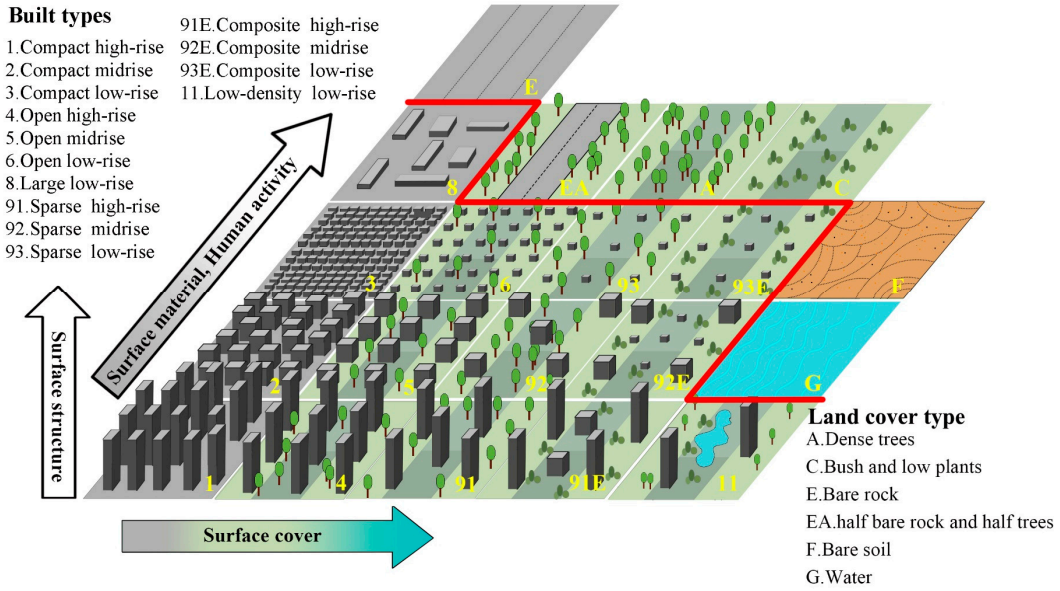


Figure 4. Various schematic diagrams of local climate zones in Changsha City.

The LCZ maps for 2005, 2010, 2015, and 2020 (Figure 5) showed an increase in built types over time, while land cover types transitioned from contiguous to fragmented patterns. Between 2010 and 2015, a significant amount of land was under construction, leading to the expansion of the LCZ-E area. But by 2020, the construction will be basically completed, with a significant reduction in the number of LCZ-E and a more diverse distribution of the LCZ types. The types of LCZ in the periphery of the central urban area will be more diverse than those in the central urban area, while the early types in the central urban area were relatively single.

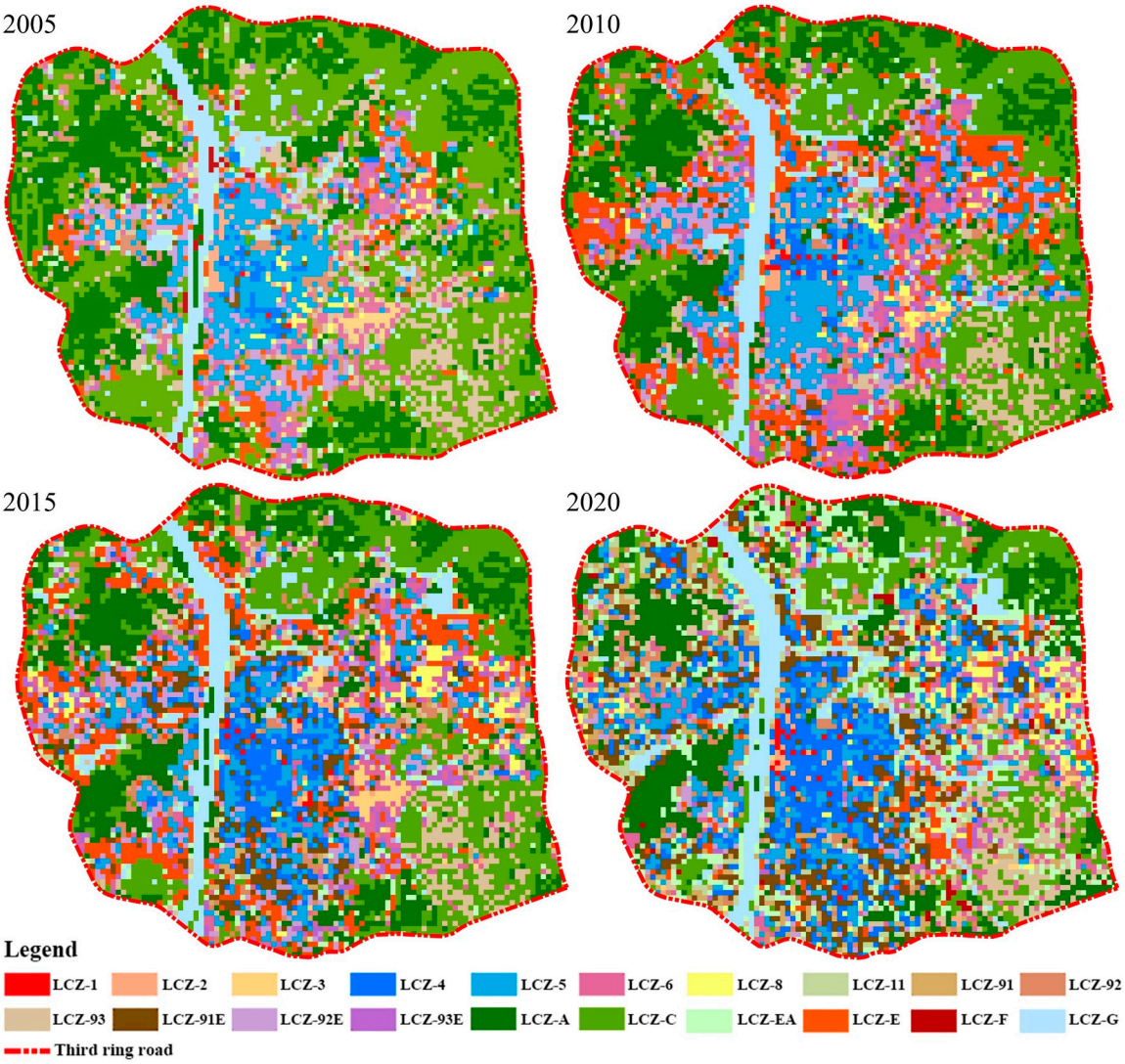


Figure 5. The LCZ maps in the years 2005, 2010, 2015, and 2020.

3.2. General Changes in LCZ

3.2.1. Quantitative Changes

Table 3 illustrates the percentage changes of each LCZ type from 2005 to 2010, 2015, and 2020. The percentage of the built LCZs rose from 32.77% to 54.38%. The proportion of the compact LCZs (LCZ 1–3) remained stable, while the open LCZs (LCZ 4–6) saw the largest increase, followed by the sparse LCZs (LCZ 91–93) and the composite LCZs (LCZ 91E–93E). The area of the LCZ-93, mostly rural villages, decreased throughout the period. The land cover LCZs overall decreased, but the LCZ-E and LCZ-EA, most of which are urban roads of squares, mainly urban roads and squares, increased.

Table 3. Yearly change rates in 2010, 2015, and 2020 compared to 2005 and overall change rate from 2005 to 2020 (%).

	1	2	3	4	5	6	8	11	91	92	93	91E	92E	93E	A	C	E	EA	F	G	Overall Change	
																					Built LCZs	Land Cover LCZs
2005	0.07	0.66	0.61	1.08	7.87	3.30	0.86	0.30	3.38	8.21	0.60	3.86	1.94	0.03	22.62	31.87	2.57	4.47	0.40	5.30	32.77	67.23
2010	0.14	0.6	−0.14	0.74	1.68	1.03	−0.08	0.01	0.01	−1.28	−1.19	0.56	2.06	2.07	−5.3	−7.97	−0.6	7.9	−0.4	0.16	38.98	61.02
2015	0.15	−0.15	0.61	4.29	−0.27	0.58	0.66	0.41	0.61	−0.66	−2.72	4.44	2.03	1.11	−6.89	−12.61	1.63	6.85	−0.4	0.16	43.86	56.14
2020	0.36	−0.01	−0.06	8.93	0.57	1.23	0.34	2.88	3.67	0.65	−3.04	7.91	−1.16	−0.66	−13.69	−25.45	0.82	16.68	0.15	−0.43	54.38	45.62

The data from 2010, 2015, and 2020 are compared to the baseline data from 2005. Positive values represent an increase in quantity. Negative values represent a decrease over the respective time periods. The overall change rate represents the annual change in the total number of LCZ types.

Appendix A illustrates the transition changes of LCZ types over the years 2005, 2010, 2015, and 2020. Colored numbers in Appendix A indicate areas where the LCZ types remained unchanged. Overall, land cover types showed greater stability, with fewer changes over time, while built types experienced more frequent transitions. This higher frequency of change in built types is mainly due to urban renewal and the introduction of new high-rise buildings. In the compact LCZs, the number of the LCZ-1 increased significantly, particularly between 2015 and 2020, mostly due to conversions from other built types. The greatest change is the open LCZs, especially the LCZ-4, which primarily transitioned from the LCZ-5 and LCZ-C. LCZ-5 and LCZ-6 showed smaller changes in quantity but experienced regional shifts, especially between 2010 and 2015, driven by urban expansion that facilitated the conversion of LCZ-C, LCZ-A, and LCZ-93 into these types. The sparse and composite LCZs, except for the LCZ-93, were mostly newly developed types resulting from urban growth. The LCZ-93, representing rural residential areas, continuously declined, with the most significant decrease occurring between 2015 and 2020. This type is mostly converted into built types, with a smaller portion transitioning to land cover types. The land cover LCZs generally retained their original types and regions more consistently than the built LCZs, indicating a more stable natural environment pattern. The main changes were seen in the LCZ-A, LCZ-C, and LCZ-G, which predominantly transitioned into the built types, as well as in the LCZ-E and LCZ-EA, where significant changes occurred between 2015 and 2020. During the rapid urban expansion between 2010 and 2015, there was a substantial increase in urban roads and other hardened surfaces, which affected the number of the LCZ-E and LCZ-EA types.

The primary LCZ changes were from land cover types to built types, with fewer reversals under the trend of urban expansion. However, a small portion of the urban areas transitioned in the opposite direction as urban villages increased. This growth affected the city's appearance, land resource allocation, and residents' quality of life. Consequently, many of these urban villages were demolished or redeveloped; some areas remained the built-up zones, while others were transformed into the land cover zones. For example, the Yazui Park in Changsha transformed from an urban village to a park.

3.2.2. Spatial Layout Changes

Comparing the LCZ maps from 2005 to 2020 in Figure 5 shows that the central urban area experienced minimal changes in the LCZ types, with the area predominantly consisting of high-rise, high-density types. In contrast, the periphery underwent more significant changes, transitioning from natural environments to built environments, mainly mid- and high-rise buildings. Therefore, three representative transects were selected to analyze the spatial changes in the LCZ types (Figure 6). Transect A-A runs east–west along Wuyi Avenue, an initial commercial hub with numerous high-rise buildings and key landmarks. Transect B-B, running east–west, passes through Meixi Lake, Yulu Mountain, Orange continent head, and Gaoqiao Big Market in an east–west direction, reflecting urban development west of the Xiangjiang River. Transect C-C, running north–south, traverses significant urban developments. Transect C-C passes through Huangxing Pedestrian Street, Wuyi Square, and runs through Binjiang Cultural Park and the composite real estate project-

Xiangjiang Century City in the north, mainly reflecting the urban construction situation in the north-south direction.

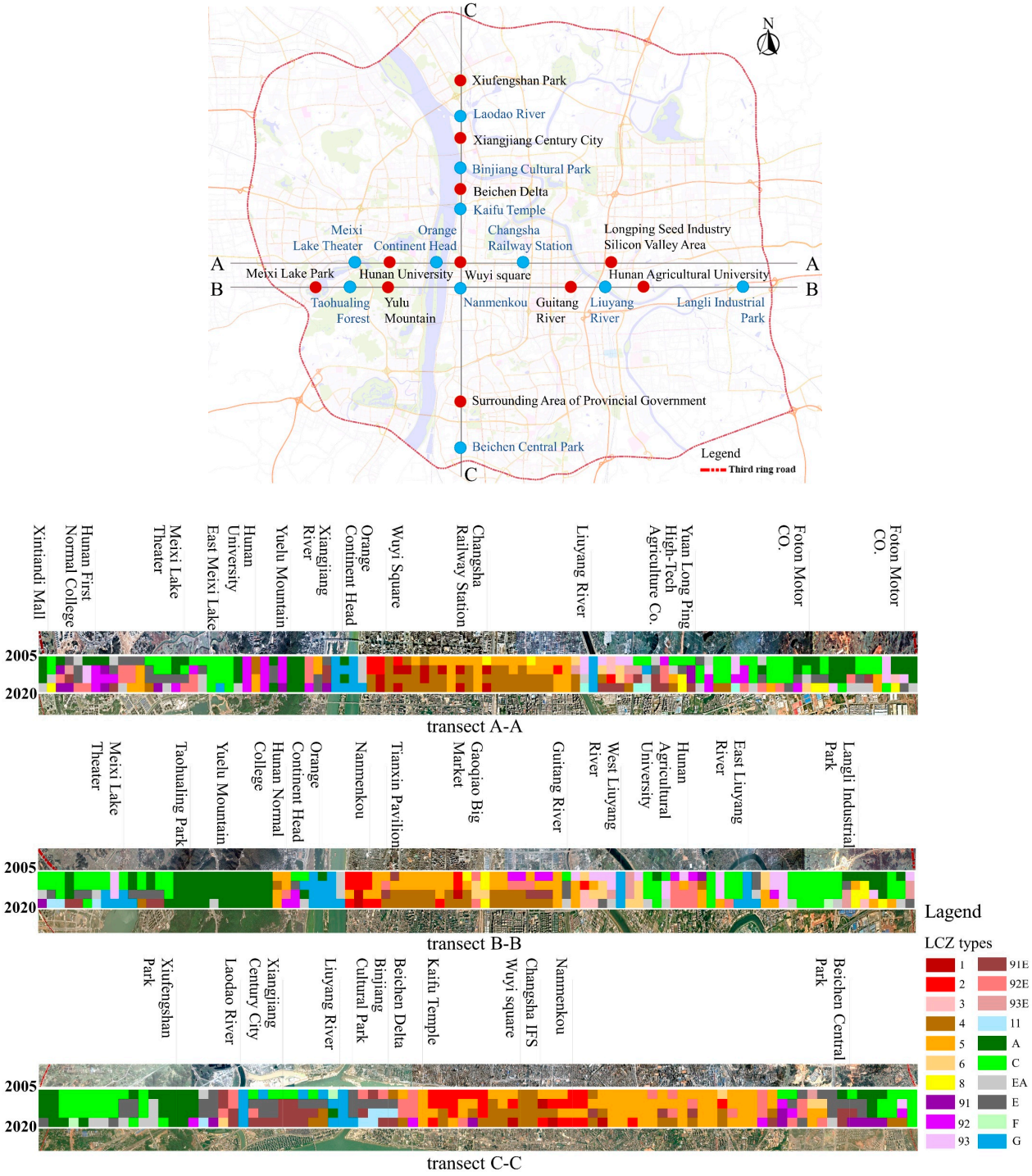


Figure 6. The spatial variation of the LCZ types from 2005 to 2020.

Figure 6 Transects illustrates the changes in the LCZ types from 2005 to 2020. The LCZ grid in the figure consists of four rows, with each row representing the LCZ types for a specific year (the first row represents 2005, and the fourth row represents 2020). Each column represents the LCZ changes for the same urban area over time. Large areas of the same color indicate that the LCZ in that region remained unchanged over time, while a column with different colors indicates that the LCZ type changed every year. In transect

A-A, before the development of Meixi Lake, the area was low-lying. After its completion in 2017, the LCZ-C transformed into the LCZ-G. To the west of Meixi Lake Theater, the LCZ-A and the LCZ-C became the LCZ-92 and the LCZ-92E. From the Xiangjiang River to the Liuyang River, the core urban area saw minor LCZ changes, mainly focused on improving quality and upgrading construction. In transect B-B, the construction of Meixi Lake Park increased the LCZ-G. Near the Third Ring Road, the LCZ types changed from the LCZ-A and the LCZ-C to the LCZ-8. In transect C-C, areas like Xiangjiang Century City and Beichen Delta shifted from the LCZ-C to the LCZ-91E. Due to the proximity of the Beicheng Delta plot to the river, the edge plot is classified as the LCZ-11.

Overall, the LCZ expansion aligns with urban structural development directions (Figure 7). In 2005, the main growth was along the Xiangjiang River and National Highway 319, forming a T-shaped pattern. By 2010, urban planning shifted to a multi-center model along Fuyong Road and Shaoshan Road. In 2015, the development axis moved to the Xiangjiang River, promoting growth on both sides. The 2020 plan continued this multi-directional expansion pattern, but its main development axis has shifted from north–south to east–west.

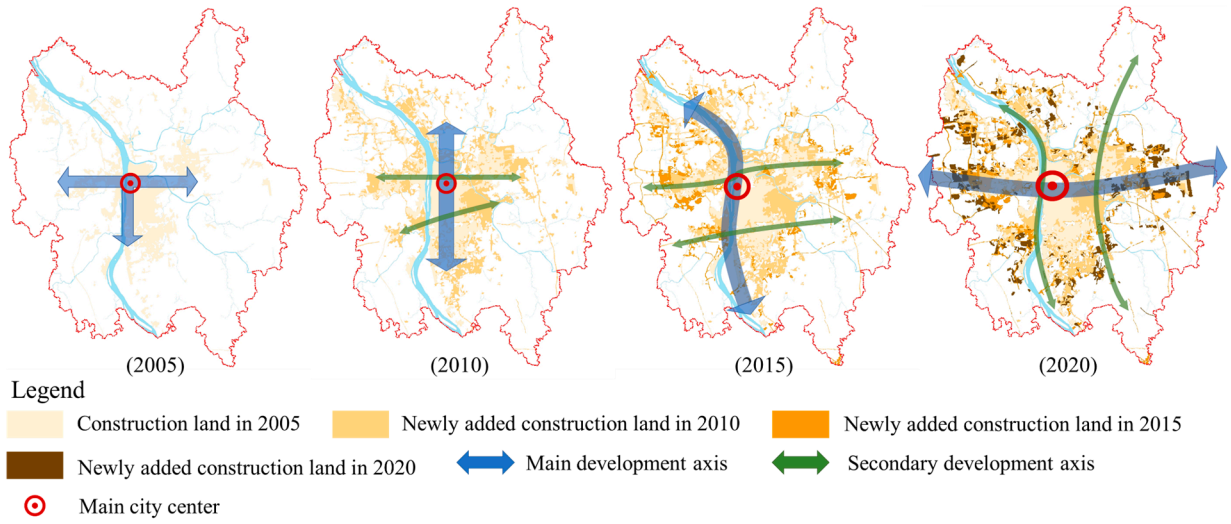


Figure 7. The urban structural development directions from 2005 to 2020.

3.3. Land Surface Temperature Analysis

Figure 8 depicts the summer and winter LST gradations within the Third Ring Road for 2005, 2010, 2015, and 2020, and Table 4 illustrates the percentage of LST gradations. In summer, high-temperature areas consistently appeared in central urban areas, industrial parks, and along major roads, while low-temperature areas were in large water bodies, forest parks, and vegetated regions outside the central urban area. As the city expanded, industrial parks, such as the Lugu High-Tech Industrial Park (A in Figure 8) and the Changsha Economic and Technological Development Zone (B in Figure 8), became high-temperature zones. The surface heat island zones, comprising a relatively high-temperature zone, high-temperature zone, and extremely high-temperature zone, significantly increased, with LST rising from 22.44% in 2005 to 31.51% in 2020. Conversely, the surface cold island zones, comprising a relatively low-temperature zone, low-temperature zone, and extremely low-temperature zone, decreased from 31.89% in 2005 to 24.57% in 2020.

In winter, the surface heat island zones were less concentrated (Figure 8e–h), scattered mainly in industrial areas, with cold islands remaining in large water bodies, forest parks, and peripheral vegetated areas. Lower overall temperatures led to less pronounced differences between the surface cold island zones and heat island zones compared to summer. The SUHI area was much smaller in winter, with proportions of 17.68% in 2005 and 18.24% in 2020, showing minor irregular changes. The surface cold island zone proportions were

higher than the SUHIs but lower than summer cold islands, as mid-temperature zones occupied more area in winter. The changes in cold islands were irregular, mostly in peripheral urban areas.

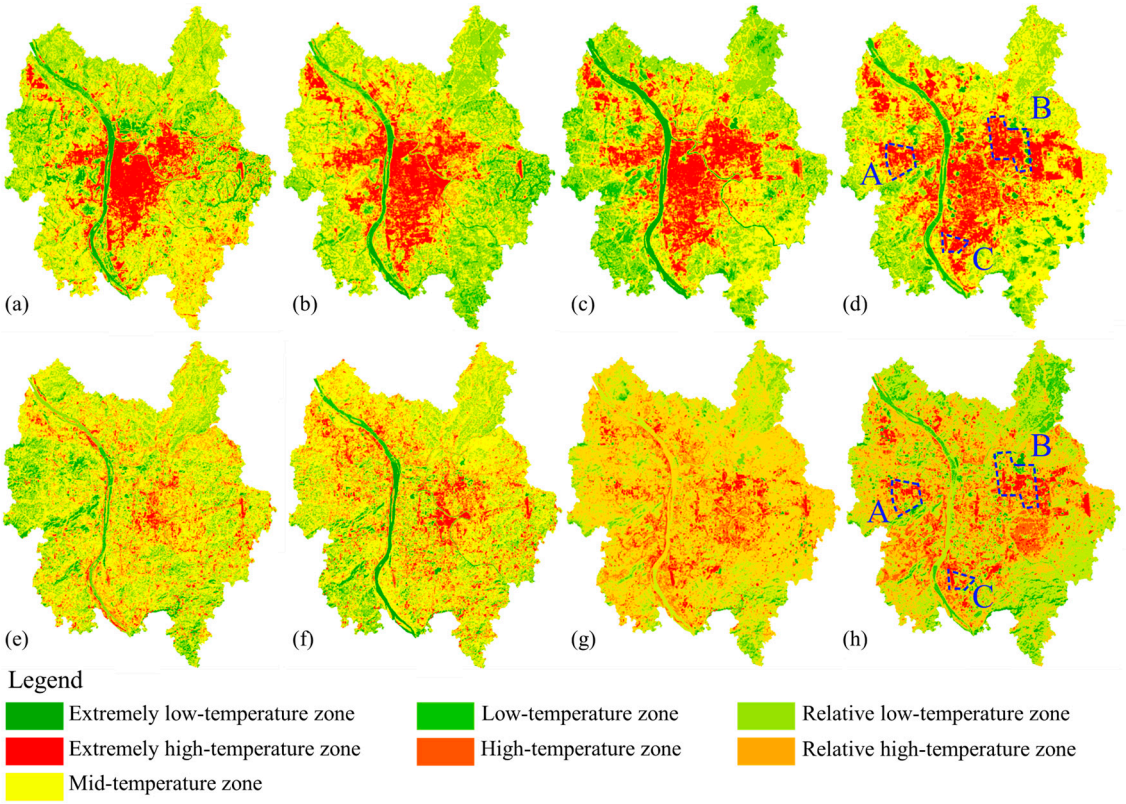


Figure 8. Spatiotemporal distribution of the LST in Changsha in summer and winter in 2005, 2010, 2016 and 2020: (**a**) 2005, (**b**) 2010, (**c**) 2016, and (**d**) 2020 in summer; (**e**) 2005, (**f**) 2010, (**g**) 2016, and (**h**) 2020 in winter; A: Lugu High-Tech Industrial Park, B: Changsha Economic and Technological Development Zone, C: Changsha Tianxin Economic Development Zone.

Table 4. Share of the LST class in the region from 2005 to 2020 (%).

LST Class		2005		2010		2016		2020	
		Sum.	Win.	Sum.	Win.	Sum.	Win.	Sum.	Win.
The surface heat island areas	Extremely high-temperature zone	11.11	2.89	9.64	4.70	10.32	3.12	11.63	4.43
	High-temperature zone	3.88	3.79	6.89	5.46	7.71	4.20	9.36	13.18
	Relatively high-temperature zone	7.45	11.00	9.77	13.52	8.46	13.14	10.52	0.63
	overall	22.44	17.68	26.30	23.68	26.49	20.46	31.51	18.24
Mid-temperature zone		45.67	53.19	35.21	54.17	33.95	53.77	43.92	35.53
The surface cold island zones	relatively low-temperature zone	20.84	21.17	29.57	14.49	27.95	20.02	17.54	35.92
	low-temperature zone	7.40	6.33	7.69	4.73	8.08	4.86	5.36	9.42
	extremely low-temperature zone	3.65	1.63	1.23	2.93	3.53	0.89	1.67	0.89
	overall	31.89	29.13	38.49	22.15	39.56	25.77	24.57	46.23

3.4. Relationship between LCZ and SUHII

Due to substantial LST differences across years, the SUHII was chosen for analysis. Figure 9 shows the SUHII changes across the LCZ types in summer and winter, with the

average SUHII values represented by lines. The summer SUHII values were much higher than in winter, with varying trends among types. In summer, the built types had average temperatures about 6 °C higher than the land cover types; in winter, the difference was around 1.5 °C.

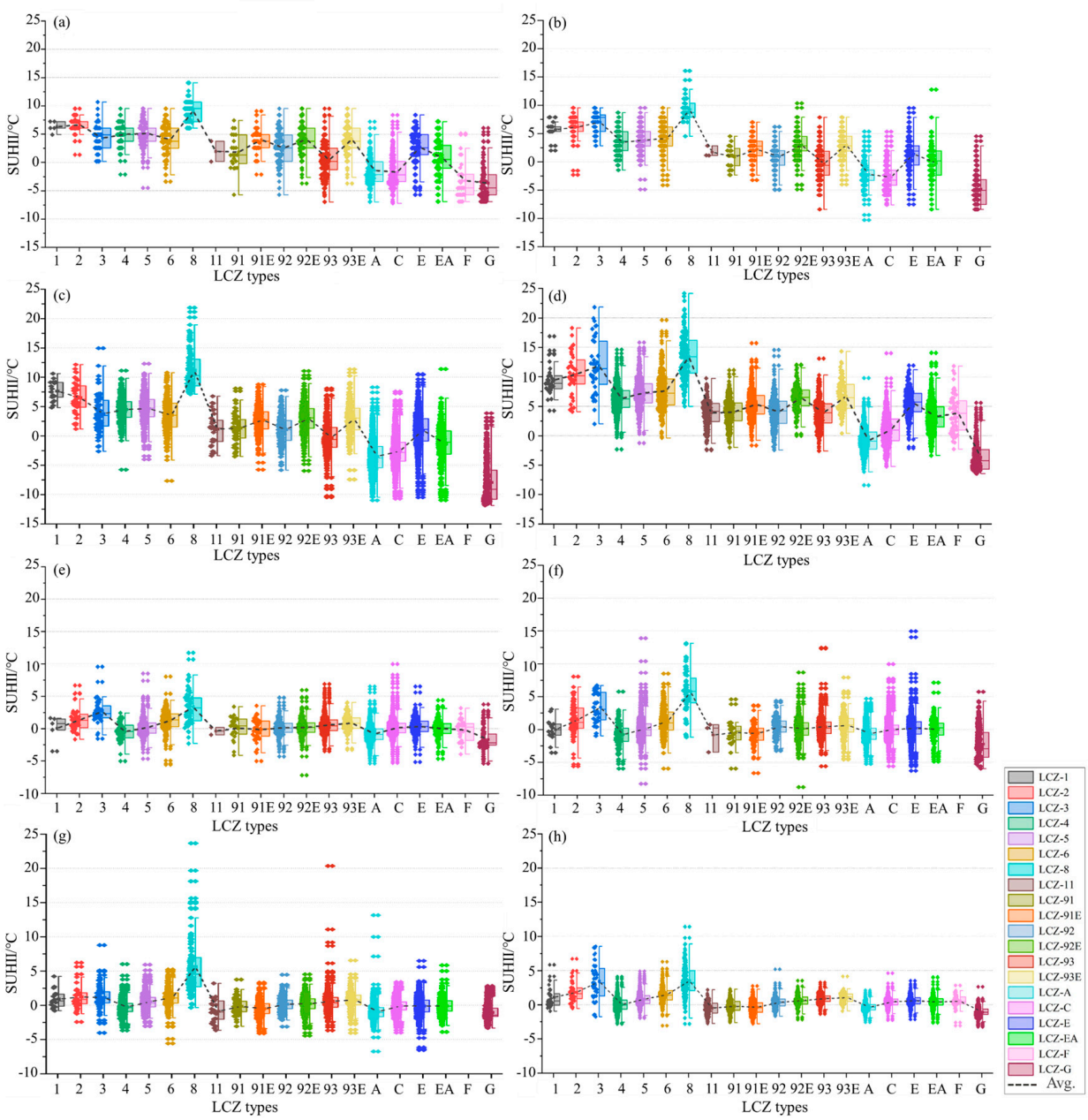


Figure 9. Changes of the SUHII in the LCZ in summer and winter in 2005, 2010, 2016, and 2020: (**a**) 2005, (**b**) 2010, (**c**) 2016, and (**d**) 2020 in summer; (**e**) 2005, (**f**) 2010, (**g**) 2016 and (**h**) 2020 in winter. The boxplots represent the variation of SUHII values for each LCZ type, while the strip plots indicate the mean SUHII value for each LCZ type.

In summer, the average SUHII values varied widely among the LCZ types. For the built types, the LCZ-8 had the highest average SUHII, while the LCZ-E had the highest among the land cover types and the LCZ-G the lowest. The SUHII trends in built types were consistent: the compact LCZs (LCZ 1–3) > the open LCZs (LCZ 4–6) > the composite LCZs (LCZ 91E–93E) > the sparse LCZs (LCZ 91–93). Among the first three, low-rise buildings had the highest SUHII, while high-rise had the lowest. For the sparse LCZs, mid-rise had

the highest SUHII, and low-rise had the lowest. In land cover types, the LCZ-E and the LCZ-F had the higher average SUHII, with the LCZ-F in the central urban area often being undeveloped plots or construction stages, leading to the high AL values and the SUHII.

In winter, the differences in SUHII values were smaller. The LCZ-8 and the LCZ-E still had the highest average SUHII, and the LCZ-G was the lowest. The SUHII trends in built types remained the same, but the low-rise buildings had the highest SUHII in each type, while the high-rise had the lowest. Differences between composite and the sparse LCZs narrowed. In the land cover types, the LCZ-E had the highest SUHII, followed by the LCZ-C and the LCZ-EA. The average values of different LCZs were closer in winter due to leaf drop and dried grass.

3.5. The Relative Importance of LCZ Parameters on Seasonal SUHI

The study used the BRT algorithm to explore the impact of LCZ parameters on the SUHII. BRT's advantage lies in handling highly non-linear relationships and interactions with less sensitivity to multicollinearity. Prior to using BRT, Variance Inflation Factor (VIF) tests ensured the model could learn meaningful relationships from the data. Typically, a VIF > 10 indicates multicollinearity [65]. Thus, FAR variables with VIF > 10 in both summer and winter were excluded. PSF and ISF, being complementary, also posed collinearity issues, so one was excluded. The remaining variables had VIF < 10, indicating no multicollinearity.

Relative importance measures a feature's impact on the model's predictive ability, assessed by the mean decrease in impurity (MDI) each feature contributes during tree splitting. The BRT model sampled 30,342 pixels to determine LCZ parameter contributions to the SUHII. Variables explained 91.10% of SUHII variation in summer and 77.77% in winter. Figure 10 ranks parameters by relative importance: in summer, ISF (35.32%) had the most influence, followed by BSF (21.61%), NDVI (12.62%), and AL (9.98%). In winter, AL (26.53%), BSF (21.22%), NDVI (12.17%), and SVF (12.10%) were most important. This indicates that impervious surfaces' warming effect outweighs vegetation cover's cooling in summer. AL and SVF variations also significantly regulate the SUHII in both seasons.

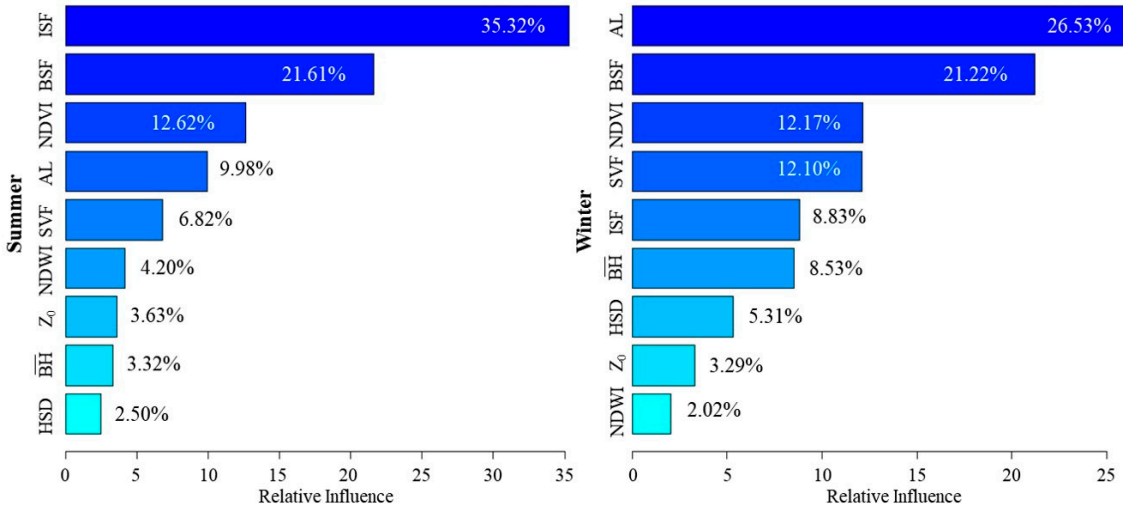


Figure 10. Relative influences of the LCZ parameters in the two seasons.

3.6. Constructing SUHI Prediction Models

3.6.1. Model Comparison and Analysis

To validate the BRT model, polynomial and spline regression models were used for cross-validation. Table 5 presents the cross-validation results, confirming the higher predictive accuracy of the BRT model compared to the others. The BRT model's R^2 values were 0.9110 for summer and 0.7777 for winter.

Table 5. Estimation results of the model.

	R^2		R^2 SD		RMSE		MAE	
	Sum.	**Win.**	**Sum.**	**Win.**	**Sum.**	**Win.**	**Sum.**	**Win.**
BRT	0.9110	0.7777	0.0021	0.0032	1.3296	0.7671	1.0435	0.5769
Polynomial Regression	0.7386	0.3494	0.0028	0.0083	2.2579	1.3098	1.7494	0.8983
Spline Regression	0.7442	0.3548	0.0031	0.0103	2.2472	1.2718	1.7301	0.8863

Figure 11 shows the BRT model's prediction results, with actual values on the *X*-axis and predicted values on the *Y*-axis. A red reference line with a slope of 1 indicates perfect predictions. The model's values align closely with the reference line, with most scatter points near a straight line, indicating accurate predictions for most observations despite some outliers.

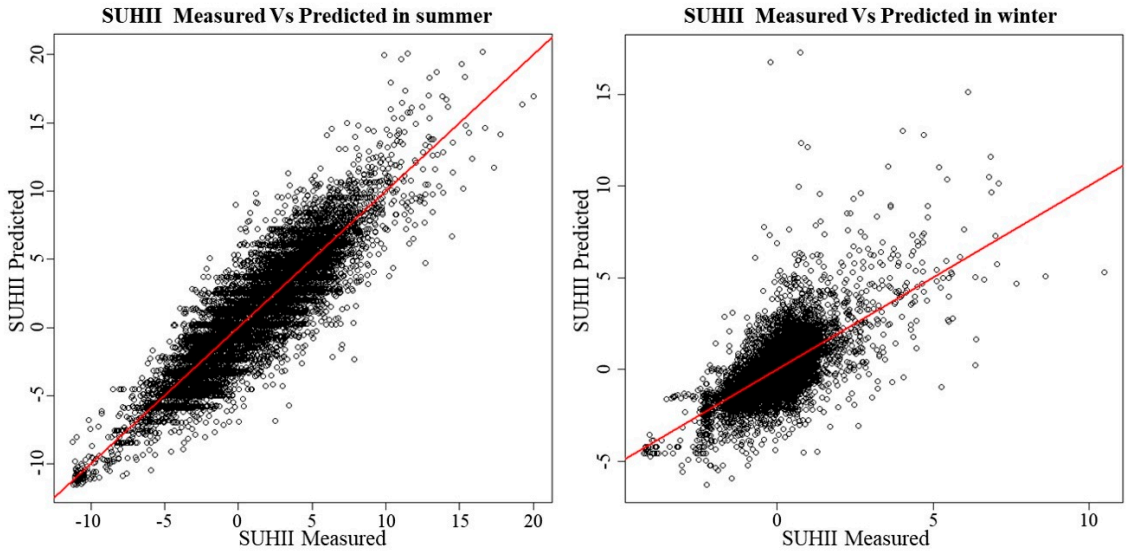


Figure 11. BRT model's prediction results.

3.6.2. Case Study Validation

To further demonstrate the prediction model's accuracy and applicability, Wangcheng District outside the Third Ring Road was chosen for application. Located northwest of Changsha, this study area covers approximately 11.43 km^2. Figure 12 shows the relationship between Wangcheng District and the Third Ring Road, and the LST in summer and winter. The R^2 values for summer (0.9786) and winter (0.9677) indicate that the model explains 97.86% and 96.77% of the SUHI variance, respectively, with higher accuracy in summer (Table 6). The relatively low RMSE and MAE values further confirm the model's small prediction errors, indicating its practical applicability in both seasons.

Table 6. Estimation results of the BRT model in Wangcheng.

	R^2	RMSE	MAE
Summer	0.9786	0.5208	0.4032
Winter	0.9677	0.2236	0.1686

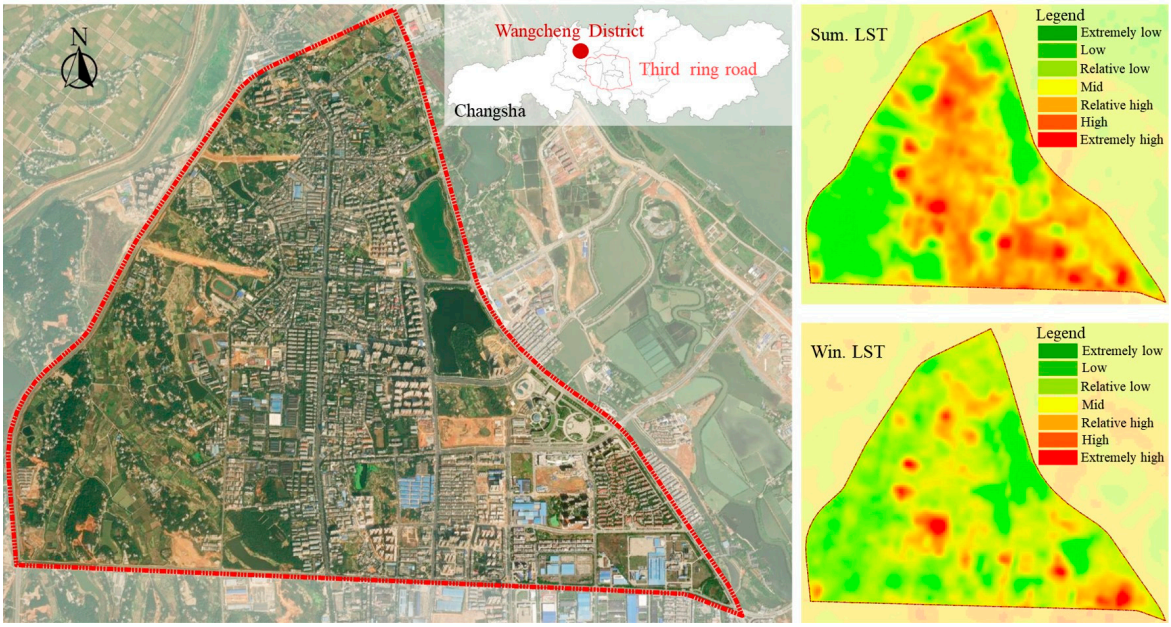


Figure 12. The location and LST of Wangcheng District.

4. Discussion

4.1. Spatial-Temporal Evolution Characteristics of the LCZ

Current studies often overlook the temporal and spatial variability of the LCZs, focusing on a single year's data to analyze the relationship between the LCZs and the LST. This approach lacks representativeness and fails to capture the dynamic relationship between changing urban spaces and temperature [19].

Our results demonstrate that the LCZ transformations are gradual. Initially, these changes are guided by urban planning objectives, but over time, they evolve into types with better permeability or high density. In China, urban planning is revised every five years, with multi-level and multi-scale features influencing the LCZ changes. For example, some areas classified as the LCZ-91E in 2015 transformed into the LCZ-91 with higher permeability by 2020. Similarly, areas categorized as the LCZ-92E transitioned into the LCZ-92, also indicating increased permeability. These changes are typical in newly developed areas where vegetation and permeable surfaces have not yet matured. As vegetation grows, the types shift to those with higher permeability indices, such as the LCZ-E transformed into the LCZ-EA. Conversely, some built types transition to higher-density types over time. For instance, the LCZ-91 and the LCZ-91E may be converted to the LCZ-4, while the LCZ-92 and the LCZ-92E may be converted to the LCZ-5. The land cover types LCZ transitioning to the built types may first become LCZ-E or LCZ-EA before fully converting to the built types. Similarly, the land cover types can transform among themselves, such as the LCZ-A becoming the LCZ-C and then the LCZ-G.

Urban expansion and quality improvements in central urban areas alter the original LCZ types, affecting the SUHI. Some LCZ types transition from built to land cover environments, while the relocation of urban functional zones also drives the LCZ changes. Areas transitioning from the built to the land cover types are mainly the LCZ-93, with some LCZ-92 and LCZ-6, and typically become parks or water bodies (LCZ-A, LCZ-C, LCZ-G), resulting in minor SUHI changes. The relocation of industrial zones is a notable example of reverse change. In 2005, industrial areas near the Second Ring Road and east of the Xiangjiang River had higher LSTs. By 2020, these zones moved to the northeast (the Changsha Economic and Technological Development Zone, B in Figure 8), south (the Changsha Tianxin Economic Development Zone, C in Figure 8), and west (the Lugu High-Tech Industrial Development Zone, A in Figure 8), altering the city's functional zones and

surface temperatures. The former industrial areas transitioning to natural or built surfaces influenced the SUHI, causing reverse changes in heat islands.

4.2. Impact of LCZ Parameter on SUHI

Optimizing urban spatial morphology is one of the most effective ways to improve the thermal environment. However, existing studies lack in-depth research on the relationship and mechanisms between urban morphology and the thermal environment. The complexity of urban spatial morphology, along with its heterogeneity and similarity, leads to both commonalities and differences in urban thermal environments. Moreover, the measurement of urban thermal environments lacks standardized indicators, with researchers from different disciplines focusing on varied metrics. For example, landscape ecology and landscape architecture emphasize landscape drivers [26], geography focuses on land cover change [66], architecture examines building morphology [67], and urban planning considers built space planning elements [37]. These differences result in non-comparable study conclusions. Therefore, this study uses the LCZ classification system to explore the relationship between urban spatial morphology parameters and the SUHI.

The BRT regression model was employed to explore the urban thermal environmental factors affecting the SUHI across the study area and the LCZ types area. BRT, involving estimates across different regression models, avoids spatial autocorrelation of indicators and explains spatial heterogeneity, effectively capturing the importance of independent variables. Due to seasonal differences in the LST and the SUHI, various LCZ types exhibit different patterns of change across seasons. Therefore, it is necessary to study the LCZ parameters separately for different seasons. Quantitative analysis revealed that building morphology significantly influences the SUHI in both summer and winter, suggesting that the replacement of vegetation with impervious surfaces and building morphology during urbanization are primary causes of the SUHI. Wherein, ISF, BSF, AL, SVF and NDVI are the key parameters affecting the SUHI in the LCZ indicators. In summer, ISF exerts the most significant influence on the SUHI, followed by BSF and NDVI. In contrast, AL and BSF play the most crucial role in regulating the SUHI in winter, followed by NDVI and SVF. This indicates that, in both summer and winter, the warming effect of impervious surfaces on the SUHI surpasses the cooling effect of vegetation and water, and the relative importance of NDVI remains consistent. The relative importance of AL is higher in winter than in summer, possibly due to the angle of solar radiation during winter affecting surface radiation absorption. Higher AL values lead to higher surface temperatures.

4.3. Impact of Urban Planning

Cities are the spatial carriers of human production and life. By 2050, 68% of the global population is expected to reside in urban areas [68]. The increase in urban population density and continuous expansion of urban construction land significantly alter surface characteristics. The replacement of natural surfaces with impervious materials like concrete and asphalt raises urban temperatures, exacerbating the urban heat island effect. The synergistic effects of heatwaves and urban heat islands further deteriorate urban thermal environments, affecting more city residents. This study, through long-term, large-scale, and multi-dimensional research, summarizes the temporal and spatial evolution of Changsha's LCZs, exploring the relationship between urban morphology and thermal environment in hot summers and cold winters, and refines the evidence-based design theory for healthy living environments. To mitigate the SUHI effect, we propose three strategies. First, zones highly susceptible to the SUHI, such as the compact-built LCZ, the open-built LCZ, and the LCZ-8, should receive special attention. Natural elements like vegetation and water bodies should be strategically distributed in these areas using a decentralized approach during urban planning [69,70], as it not only isolates urban heat but also helps in constructing urban wind corridors. Alternatively, these zones can be converted to low SUHI zones, like the sparse-built LCZ or the composite-built LCZ. Second, new area planning should strictly control the LCZ types, favoring those with low SUHIs. Low AL materials should be

selected for construction and surface cover, increasing permeable surfaces and encouraging rooftop and wall greening. Building density and height should be carefully planned, particularly in industrial areas, to prevent excessive concentration of heat-generating regions. Third, the SUHI mitigation strategies should be integrated during the planning design stage. We propose a more precise and convenient method for assessing thermal environments, which can be used to evaluate the SUHI during the concept planning phase. This predictive model allows for adjustments in the design stage and provides guidance for the subsequent detailed planning to achieve sustainable urban development. The method requires relatively low expertise and operational costs, making it practical for urban planners.

4.4. Limitations

The LCZ-based SUHI analysis shown in this study can be extended to other cities with similar climatic conditions or even a national scale, provided the LCZ data and surface temperatures are available. Although this methodology detects intra-urban thermal variations and crucial heat islands, some limitations remain. Firstly, besides the LCZ scheme, many scholars use the urban functional zones and urban blocks as research units, effectively applying them in city management activities like urban planning, heat vulnerability assessment, and energy conservation promotion. In China's current territorial spatial planning system, planning is based on block units. Further exploration is needed to determine which LCZ division method best suits Chinese cities. Secondly, the quality and resolution of Landsat image data pose challenges. The periodicity and spatial granularity of Landsat data limit studies to daytime data in the same month, excluding the nighttime SUHI research. More thermal earth observation missions and higher-resolution satellite images are needed to improve accuracy. Furthermore, since Changsha has distinct hot summers and cold winters, this study only focused on these seasons. Future studies in other cities, especially subtropical ones, should include spring and autumn to understand the SUHI variations during transitional seasons. Finally, the SUHIs are closely related to the thermal comfort of residents. In addition to physiological factors, psychological factors should also be considered [71]. Future research will incorporate additional influencing factors to refine the prediction models.

5. Conclusions

This study focused on Changsha, a representative high-temperature city. Using the LCZ scheme, it described the SUHI distribution across different years and seasons, clarifying the temporal and spatial evolution of the LCZs and the SUHI. It also elucidated the non-linear relationship between the spatial parameters and the SUHI, mapping the connection between urban planning and the urban thermal environment. The main conclusions are as follows: (1) Through long-term analysis, a localized LCZ classification system for Changsha was constructed, and the spatial-temporal changes of LCZs from 2005 to 2020 were analyzed. The number of built-type LCZs increased from 32.76% to 54.38%, with few maintaining their original type and most undergoing multiple changes. The spatial layout shifted from contiguous single types to mixed distributions, radiating outward. The number of land cover type LCZs decreased, with fewer transitions from the built type LCZs, changing from contiguous to clustered layouts. (2) Changsha's SUHI shows an upward trend, with varying changes in the built-type LCZs between summer and winter and notable differences among the LCZ types. In summer, the SUHI trend for the built type LCZs is the LCZ-8 > the compact LCZ > the open LCZ > the composite LCZ > the sparse LCZ > the LCZ-11, with different changes among the high-rise, the mid-rise, and the low-rise types. In winter, the differences are smaller, with similar trends among the LCZ types. (3) Using the BRT model, a more accurate and convenient SUHI prediction method was constructed. The BRT model's relative importance analysis indicated that building morphology and surface materials are the main parameters affecting the SUHI in both summer and winter. The constructed SUHI assessment equation showed high pre-

dictive accuracy, with R^2 values of 0.911 for summer and 0.777 for winter. Case validation demonstrated the model's ability to explain 97.86% (summer) and 96.77% (winter) of the data. (4) The high-temperature clusters in the study area are mainly the LCZ-8, the compact LCZ, and the LCZ-E, characterized by high impervious surfaces. These areas should be prioritized for urban renewal efforts, focusing on transforming them into open, high-rise modern communities.

Author Contributions: Conceptualization, Y.X.; methodology, Y.X. and J.Z; software, Y.X., J.G. and J.W.; validation, Y.X. and J.G.; formal analysis, Y.X. and J.W.; visualization, Y.X., J.Z. and J.G.; investigation, Y.X., J.G. and J.W.; writing—original draft preparation, Y.X.; writing—review and editing, J.Z. and B.Z.; supervision, B.Z.; funding acquisition, Y.X. and B.Z. All authors have read and agreed to the published version of the manuscript.

Funding: This research was funded by Hunan Provincial Natural Science Foundation General Project [No. 2023JJ30693], Hunan Provincial Social Science Achievement Evaluation Committee Key Project [No. XSP20ZDI021], Hunan Provincial Philosophy and Social Science Planning Fund Office [No. CX20220123].

Data Availability Statement: The data presented in this study are available on request from the corresponding authors due to privacy.

Conflicts of Interest: The authors declare that they have no known competing financial interests or personal relationships that could have appeared to influence the work reported in this paper.

Appendix A

Table A1. LCZ transformation of the region from 2005 to 2010.

LCZ Class		2010																				
		1	**2**	**3**	**4**	**5**	**6**	**8**	**11**	**91**	**92**	**93**	**91E**	**92E**	**93E**	**A**	**C**	**E**	**EA**	**F**	**G**	**OA (2005)**
2005	1	1	2		1	1																5
	2	4	36	1		5	1	4														51
	3		20	14				13														47
	4	2	2		47	26	2						2					2				83
	5	8	23	2	49	464	20	10			2		4	16	4			1	1			604
	6		3	8	1	41	183	7						3	6			1				253
	8	1	7	8	2	15	10	16				1		3	2			1				66
	11								1				1									2
	91				3	3				5			9	2							1	23
	92			1	3	32	7	2		2	78	3	5	109	2	3	1	9	2			259
	93					14	30	1			12	425		26	112		1	5				626
	91E				7	5	1						27	5				1				46
	92E		1	1	10	63	18			1	11	3	6	165	9			7	1			296
	93E			1	2	9	21				2	10	1	11	83			8				148
	A		3		1	11	7	2		5	19	28	10	27	23	1231	34	239	39		21	1700
	C				6	18	18	2		3	25	43	7	42	30	42	1740	322	62		42	2402
	E				6	20	9	3	1	1	2	11	15	37	24	7	8	190	2		1	337
	EA				2	5	5			4	7	7	2	7	7	9	10	103	23		2	193
	F																	2			28	30
	G					1			1	3	3	3		1	2	7	10	39	14		321	405
	OA (2010)	16	97	36	140	733	332	60	3	24	161	534	89	454	304	1299	1804	930	144	0	416	7576

Row refers to the number of LCZ classified in 2005. Column refers to the number of LCZ classified in 2010. OA (2005) refers to the overall of each LCZ class in 2005. OA (2010) refers to the overall of each LCZ class in 2010. Color-coded numbers indicate instances where the LCZ class remained unchanged.

Table A2. LCZ transformation of the region from 2010 to 2015.

LCZ Class		2015																			
		1	**2**	**3**	**4**	**5**	**6**	**8**	**11**	**91**	**92**	**93**	**91E**	**92E**	**93E**	**A**	**C**	**E**	**EA**	**G**	**OA (2010)**
2010	1	5	1		10																16
	2	6	19	25	16	23	3	3					2								97
	3	3	6	16		4	1	3					1					2			36
	4		2		92	22				2			21	1							140
	5		2	2	205	360	48	21	1	1	2		41	41	2			7			733
	6	1	2	8	38	79	134	19			2	5	14	14	7			9			332
	8	2	5	19	3	2	4	21						2				1	1		60
	11								1				1				1				3
	91								3	5	9	1		3		2			1		24
	92		1	1	2	6	3		1	16	84	17	3	12	3	5	3	1	2	1	161
	93		1	3	1	2	18	1		26	75	336	7	6	24	5	19	1	6	3	534
	91E				3	4			2				51	22	1			6			89
	92E				20	34	7	7	1		1		115	226	29			14			454
	93E			2	6	16	9	12	1	1	1		56	79	100			21			304
	A			3	2	3	13	1	5	8	13	16	5	1	3	1118	7	63	37	1	1299
	C			11	1	10	26	5	3	3	8	34	8	5	8	18	1416	133	63	52	1804
	E			3	11	15	20	33	13	4	8	4	62	39	50			561	107		930
	EA			1	2	3	2	1	2	4	4	3			1	2	4	22	93		144
	G								1		1	1		1		33	2	4	2	371	416
	OA (2015)	17	39	94	412	583	288	127	34	70	208	417	387	452	228	1183	1452	845	312	428	7576

Row refers to the number of LCZ classified in 2010. Column refers to the number of LCZ classified in 2015. OA (2010) refers to the overall of each LCZ class in 2010. OA (2015) refers to the overall of each LCZ class in 2015. Color-coded numbers indicate instances where the LCZ class remained unchanged.

Table A3. LCZ transformation of the region from 2015 to 2020.

LCZ Class		2020																			
		1	**2**	**3**	**4**	**5**	**6**	**8**	**11**	**91**	**92**	**93**	**91E**	**92E**	**93E**	**A**	**C**	**E**	**EA**	**F**	**G**	**OA (2015)**
2015	1	7			7								3									17
	2	1	12		3	12		2		2			4				1		2			39
	3	1	2	9	5	1	4	14	12	2	1	2	14	3	2		7	10	5			94
	4	20	4		341	8			4	5			28	1					1			412
	5	2	20	1	81	406	12	6		4	11	1	8	23	1			3	4			583
	6			13	13	26	121	16	7	3	2	6	13	4	7		7	25	25			288
	8	2	1	12	4	10	24	71				1			2							127
	11				5				13	2			13						1			34
	91				10	2			6	20	2		21				1	2	6			70
	92				9	13	3		4	18	80	4	11	29	3	12	1	2	18	1		208
	93				5	7	63		4	12	14	191	7	4	26	8	21	9	38	3	5	417
	91E				110	3			17	50	2		193	2				6	4			387
	92E				60	80	6	6	5	25	69	2	60	98	4	2	1	17	17			452
	93E		1	1	18	11	28	9	3	5	11	24	17	7	34		7	25	27			228
	A		3		7	9	15	5	19	34	32	38	21	1	1	700	77	10	148	24	39	1183
	C			2	13	12	17	4	35	51	39	92	34	6	10	188	586	29	272	20	42	1452
	E			2	68	34	12	8	68	53	25	20	181	23	5	25	25	85	180	7	24	845
	EA				9	9	5	2	18	17	17	7	23	3	1	30	33	16	72	4	46	312
	F																					0
	G								8	1	3	4	2	1	1	7	23	2	28		348	428
	OA (2020)	33	43	40	768	643	310	143	223	304	308	392	653	205	97	972	790	241	848	59	504	7576

Row refers to the number of LCZ classified in 2015. Column refers to the number of LCZ classified in 2020. OA (2015) refers to the overall of each LCZ class in 2015. OA (2020) refers to the overall of each LCZ class in 2020. Color-coded numbers indicate instances where the LCZ class remained unchanged.

Table A4. LCZ transformation of the region from 2005 to 2020.

LCZ Class		2020																			
		1	**2**	**3**	**4**	**5**	**6**	**8**	**11**	**91**	**92**	**93**	**91E**	**92E**	**93E**	**A**	**C**	**E**	**EA**	**F**	**G**	**OA (2005)**
2005	1	2			2	1																5
	2	8	12	2	10	10	1		3	3			1	1								51
	3		1	2	4	1	1	5	7			1	13	1	1			7	3			47
	4	2	2		66	6				2			5									83
	5	15	12		238	245	18	7	4	4	10	2	31	9	1		1	5	2			604
	6	3	1	5	42	42	43	15	10	5		1	30	6	5		4	24	17			253
	8	1	4	3	19	9	1	11	1	4	2	1	7	1	1			1				66
	11				1					1												2
	91				3	3			1	4	5	1	4					1	1			23
	92			2	41	34	11	1	2	26	43	5	46	18	5	7	1	6	11			259
	93		2	4	29	33	66	2	24	28	36	174	39	20	27	7	29	30	67	3	6	626
	91E				15	5	2		2	5	2		9	5				1				46
	92E		1		58	75	3	4	3	17	31	3	56	34	3	2		3	3			296
	93E			1	23	16	17	8	2	8	8	3	27	13	4	1	1	6	9		1	148
	A		5	5	67	48	46	32	38	68	69	60	121	20	7	729	90	34	211	25	25	1700
	C	2	3	11	100	71	80	48	84	100	72	119	161	48	35	200	635	75	399	27	132	2402
	E			3	31	33	16	7	16	18	17	10	61	13	8	12	3	21	49	3	16	337
	EA			2	14	10	4	2	13	8	9	8	23	12		9	12	11	39		17	193
	F								1								2		2		25	30
	G				5	1	1	1	12	3	4	4	19	4		5	12	16	35	1	282	405
	OA (2020)	33	43	40	768	643	310	143	223	304	308	392	653	205	97	972	790	241	848	59	504	7576

Row refers to the number of LCZ classified in 2005. Column refers to the number of LCZ classified in 2020. OA (2005) refers to the overall of each LCZ class in 2005. OA (2020) refers to the overall of each LCZ class in 2020. Color-coded numbers indicate instances where the LCZ class remained unchanged.

Appendix B

Table A5. The transformation of land cover types in the region from 2005 to 2010 (km^2).

Land Cover		2005		2010		2015		2020	
PSF	Cropland	268.15	39.43%	185.18	27.23%	156.55	23.02%	93.37	13.73%
	Forest	169.61	24.94%	134.92	19.84%	126.90	18.66%	122.27	17.98%
	Grassland	1.97	0.29%	1.70	0.25%	1.43	0.21%	1.16	0.17%
	Water	47.54	6.99%	43.73	6.43%	43.25	6.36%	42.23	6.21%
	Barren	3.33	0.49%	0	0	0	0	32.98	4.85%
	Overall	490.60	72.14%	365.53	53.75%	328.13	48.25%	292.02	42.94%
ISF		189.46	27.86%	314.53	46.25%	351.93	51.75%	388.04	57.06%

References

1. Masson-Delmotte, V.; Pörtner, H.O.; Skea, J.; Zhai, P.; Roberts, D. *Special Report: Global Warming of 1.5 °C*; Intergovernmental Panel on Climate Change (IPCC): New York, NY, USA, 2019.
2. China Meteorological Administration. *Blue Book on Climate Change in China 2023*; Science Press: Beijing, China, 2023.
3. Aerospace Information Research Institute, Chinese Academy of Sciences. Remote Sensing Monitoring Database for the Expansion of Typical Cities in China in the Past 50 Years. Available online: https://aircas.cas.cn/dtxw/kydt/202103/t20210304_5969166.html (accessed on 8 August 2023).
4. He, B.; Wang, J.; Zhu, J.; Qi, J. Beating the urban heat: Situation, background, impacts and the way forward in China. *Renew. Sustain. Energy Rev.* **2022**, *161*, 112350. [CrossRef]
5. Schwarz, N.; Schlink, U.; Franck, U.; Großmann, K. Relationship of land surface and air temperatures and its implications for quantifying urban heat island indicators—An application for the city of Leipzig (Germany). *Ecol. Indic.* **2012**, *18*, 693–704. [CrossRef]
6. Sheng, L.; Tang, X.; You, H.; Gu, Q.; Hu, H. Comparison of the urban heat island intensity quantified by using air temperature and Landsat land surface temperature in Hangzhou, China. *Ecol. Indic.* **2017**, *72*, 738–746. [CrossRef]
7. Kikon, N.; Singh, P.; Singh, S.K.; Vyas, A. Assessment of urban heat islands (UHI) of Noida City, India using multi-temporal satellite data. *Sustain. Cities Soc.* **2016**, *22*, 19–28. [CrossRef]

8. dos Santos, A.R.; de Oliveira, F.S.; da Silva, A.G.; Gleriani, J.M.; Gonçalves, W.; Moreira, G.L.; Silva, F.G.; Branco, E.R.F.; Moura, M.M.; da Silva, R.G.; et al. Spatial and temporal distribution of urban heat islands. *Sci. Total Environ.* **2017**, *605–606*, 946–956. [CrossRef]
9. Tao, S.; Ranhao, S.; Liding, C. The Trend Inconsistency between Land Surface Temperature and Near Surface Air Temperature in Assessing Urban Heat Island Effects. *Remote Sens.* **2020**, *12*, 1271. [CrossRef]
10. Xiang, Y.; Zheng, B.; Bedra, K.B.; Ouyang, Q.; Liu, J.; Zheng, J. Spatial and seasonal differences between near surface air temperature and land surface temperature for Urban Heat Island effect assessment. *Urban Clim.* **2023**, *52*, 101745. [CrossRef]
11. Stewart, I.D.; Oke, T.R. Local Climate Zones for Urban Temperature Studies. *Bull. Amer. Meteor. Soc.* **2012**, *93*, 1879–1900. [CrossRef]
12. Bechtel, B.; Alexander, P.J.; Beck, C.; Böhner, J.; Brousse, O.; Ching, J.; Demuzere, M.; Fonte, C.; Gál, T.; Hidalgo, J.; et al. Generating WUDAPT Level 0 data—Current status of production and evaluation. *Urban Clim.* **2019**, *27*, 24–45. [CrossRef]
13. Yoo, C.; Han, D.; Im, J.; Bechtel, B. Comparison between convolutional neural networks and random forest for local climate zone classification in mega urban areas using Landsat images. *ISPRS J. Photogramm. Remote Sens.* **2019**, *157*, 155–170. [CrossRef]
14. Zheng, Y.; Ren, C.; Xu, Y.; Wang, R.; Ho, J.; Lau, K.; Ng, E. GIS-based mapping of Local Climate Zone in the high-density city of Hong Kong. *Urban Clim.* **2018**, *24*, 419–448. [CrossRef]
15. Gál, T.; Bechtel, B.; Unger, J. Comparison of two different Local Climate Zone mapping methods. In Proceedings of the ICUC9—9th International Conference on Urban Climate Jointly with 12th Symposium on the Urban Environment, Toulouse, France, 20–24 July 2015.
16. Ren, C.; Wang, R.; Cai, M.; Xu, Y.; Ng, E. The Accuracy of LCZ maps Generated by the World Urban Database and Access Portal Tools (WUDAPT) Method: A Case Study of Hong Kong. In Proceedings of the 4th Countering Urban Heat Island (Uhi) and Climate Change Through Mitigation and Adaptation, Singapore, 30 May–1 June 2016.
17. Wang, R.; Ren, C.; Xu, Y.; Lau, K.K.; Shi, Y. Mapping the local climate zones of urban areas by GIS-based and WUDAPT methods: A case study of Hong Kong. *Urban Clim.* **2018**, *24*, 567–576. [CrossRef]
18. Han, J.; Liu, J.; Liu, L.; Ye, Y. Spatiotemporal Changes in the Urban Heat Island Intensity of Distinct Local Climate Zones: Case Study of Zhongshan District, Dalian, China. *Complexity* **2020**, 8820338. [CrossRef]
19. Wang, R.; Voogt, J.; Ren, C.; Ng, E. Spatial-temporal variations of surface urban heat island: An application of local climate zone into large Chinese cities. *Build. Environ.* **2022**, *222*, 109378. [CrossRef]
20. Chen, Y.; Hu, Y. The urban morphology classification under local climate zone scheme based on the improved method—A case study of Changsha, China. *Urban Clim.* **2022**, *45*, 101271. [CrossRef]
21. Ren, C.; Cai, M.; Li, X.; Zhang, L.; Wang, R.; Xu, Y.; Ng, E. Assessment of Local Climate Zone Classification Maps of Cities in China and Feasible Refinements. *Sci. Rep.* **2019**, *9*, 18848. [CrossRef]
22. Han, B.; Luo, Z.; Liu, Y.; Zhang, T.; Yang, L. Using Local Climate Zones to investigate Spatio-temporal evolution of thermal environment at the urban regional level: A case study in Xi'an, China. *Sustain. Cities Soc.* **2022**, *76*, 103495. [CrossRef]
23. Geletič, J.; Lehnert, M.; Dobrovolný, P. Land Surface Temperature Differences within Local Climate Zones, Based on Two Central European Cities. *Remote Sens.* **2016**, *8*, 788. [CrossRef]
24. Das, M.; Das, A. Assessing the relationship between local climatic zones (LCZs) and land surface temperature (LST)—A case study of Sriniketan-Santiniketan Planning Area (SSPA), West Bengal, India. *Urban Clim.* **2020**, *32*, 100591. [CrossRef]
25. Hu, J.; Yang, Y.; Pan, X.; Zhu, Q.; Zhan, W.; Wang, Y.; Ma, W. Analysis of the Spatial and Temporal Variations of Land Surface Temperature Based on Local Climate Zones: A Case Study in Nanjing, China. *IEEE J. Sel. Top. Appl. Earth Obs. Remote Sens.* **2019**, *12*, 4213–4223. [CrossRef]
26. Lin, Z.; Xu, H.; Yao, X.; Yang, C.; Yang, L. Exploring the relationship between thermal environmental factors and land surface temperature of a "furnace city" based on local climate zones. *Build. Environ.* **2023**, *243*, 110732. [CrossRef]
27. Yu, Z.; Jing, Y.; Yang, G.; Sun, R. A New Urban Functional Zone-Based Climate Zoning System for Urban Temperature Study. *Remote Sens.* **2021**, *13*, 251. [CrossRef]
28. Middel, A.; Häb, K.; Brazel, A.J.; Martin, C.A.; Guhathakurta, S. Impact of urban form and design on mid-afternoon microclimate in Phoenix Local Climate Zones. *Landsc. Urban Plan.* **2014**, *122*, 16–28. [CrossRef]
29. Chen, W.; Zhang, J.; Shi, X.; Liu, S. Impacts of Building Features on the Cooling Effect of Vegetation in Community-Based MicroClimate: Recognition, Measurement and Simulation from a Case Study of Beijing. *IJERPH* **2020**, *17*, 8915. [CrossRef] [PubMed]
30. Qiao, Z.; Xu, X.; Wu, F.; Luo, W.; Wang, F.; Liu, L.; Sun, Z. Urban ventilation network model: A case study of the core zone of capital function in Beijing metropolitan area. *J. Clean. Prod.* **2017**, *168*, 526–535. [CrossRef]
31. Han, D.; An, H.; Wang, F.; Xu, X.; Qiao, Z.; Wang, M.; Sui, X.; Liang, S.; Hou, X.; Cai, H.; et al. Understanding seasonal contributions of urban morphology to thermal environment based on boosted regression tree approach. *Build. Environ.* **2022**, *226*, 109770. [CrossRef]
32. Li, H.; Li, Y.; Wang, T.; Wang, Z.; Gao, M.; Shen, H. Quantifying 3D building form effects on urban land surface temperature and modeling seasonal correlation patterns. *Build. Environ.* **2021**, *204*, 108132. [CrossRef]
33. Hu, Y.; Dai, Z.; Guldmann, J. Modeling the impact of 2D/3D urban indicators on the urban heat island over different seasons: A boosted regression tree approach. *J. Environ. Manag.* **2020**, *266*, 110424. [CrossRef]

34. Chen, J.; Zhan, W.; Du, P.; Li, L.; Li, J.; Liu, Z.; Huang, F.; Lai, J.; Xia, J. Seasonally disparate responses of surface thermal environment to 2D/3D urban morphology. *Build. Environ.* **2022**, *214*, 108928. [CrossRef]
35. Wang, Q.; Wang, X.; Meng, Y.; Zhou, Y.; Wang, H. Exploring the impact of urban features on the spatial variation of land surface temperature within the diurnal cycle. *Sustain. Cities Soc.* **2023**, *91*, 104432. [CrossRef]
36. Li, Z.; Hu, D. Exploring the relationship between the 2D/3D architectural morphology and urban land surface temperature based on a boosted regression tree: A case study of Beijing, China. *Sustain. Cities Soc.* **2022**, *78*, 103392. [CrossRef]
37. Xu, H.; Li, C.; Hu, Y.; Li, S.; Kong, R.; Zhang, Z. Quantifying the effects of 2D/3D urban landscape patterns on land surface temperature: A perspective from cities of different sizes. *Build. Environ.* **2023**, *233*, 110085. [CrossRef]
38. Xu, Y.; Zhang, C.; Hou, W. Modeling of Daytime and Nighttime Surface Urban Heat Island Distribution Combined with LCZ in Beijing, China. *Land* **2022**, *11*, 2050. [CrossRef]
39. Yu, S.; Chen, Z.; Yu, B.; Wang, L.; Wu, B.; Wu, J.; Zhao, F. Exploring the relationship between 2D/3D landscape pattern and land surface temperature based on explainable eXtreme Gradient Boosting tree: A case study of Shanghai, China. *Sci. Total Environ.* **2020**, *725*, 138229. [CrossRef] [PubMed]
40. Alahuhta, J.; Antikainen, H.; Hjort, J.; Helm, A.; Heino, J. Current climate overrides historical effects on species richness and range size of freshwater plants in Europe and North America. *J. Ecol.* **2020**, *108*, 1262–1275. [CrossRef]
41. Han, D.; An, H.; Cai, H.; Wang, F.; Xu, X.; Qiao, Z.; Jia, K.; Sun, Z.; An, Y. How do 2D/3D urban landscapes impact diurnal land surface temperature: Insights from block scale and machine learning algorithms. *Sustain. Cities Soc.* **2023**, *99*, 104933. [CrossRef]
42. Changsha Municipal, Gov. Overview of Changsha. Available online: http://www.changsha.gov.cn/xfzs/zjmlzs/zsgl/200907/t20090727_5686409.html?eqid=dab79ba600213c5a0000000664552691 (accessed on 24 May 2024).
43. Beck, H.E.; McVicar, T.R.; Vergopolan, N.; Berg, A.; Lutsko, N.J.; Dufour, A.; Zeng, Z. High-resolution (1 km) Köppen-Geiger maps for 1901–2099 based on constrained CMIP6 projections. *Sci. Data* **2023**, *10*, 724. [CrossRef]
44. Hunan Meteorological Bureau. The Hot and Humid Competition in North China, Northeast China, and Many Places in Jiangnan May Break Records again due to High Temperatures. Available online: http://hn.cma.gov.cn/xwzx/tqzx/201808/t20180801_841310.html (accessed on 8 August 2023).
45. Colaninno, N.; Morello, E. Towards an operational model for estimating day and night instantaneous near-surface air temperature for urban heat island studies: Outline and assessment. *Urban Clim.* **2022**, *46*, 101320. [CrossRef]
46. Qin, J.; He, M.; Jiang, H.; Lu, N. Reconstruction of 60-year (1961–2020) surface air temperature on the Tibetan Plateau by fusing MODIS and ERA5 temperatures. *Sci. Total Environ.* **2022**, *853*, 158406. [CrossRef]
47. Li, Z.H.; He, W.; Cheng, M.; Hu, J.X.; Yang, G.Y.; Zhang, H.Y. SinoLC-1: The first 1 m resolution national-scale land-cover map of China created with a deep learning framework and open-access data. *Earth Syst. Sci. Data* **2023**, *15*, 4749–4780. Available online: https://zenodo.org/records/8214871 (accessed on 8 August 2023). [CrossRef]
48. Shi, Q.; Liu, M.X.; Marinoni, A.; Liu, X. UGS-1m: Fine-grained urban green space mapping of 31 major cities in China based on the deep learning framework. *Sci. Data Bank* **2023**. [CrossRef]
49. Liang, S. Narrowband to broadband conversions of land surface albedo I: Algorithms. *Remote Sens. Environ.* **2001**, *76*, 213–238. [CrossRef]
50. Davenport, A.G.; Grimmond, C.; Oke, T.R.; Wiering, J. Estimating the roughness of cities and sheltered country. In Proceedings of the 12th Conference on Applied Climatology, Asheville, NC, USA, 8–12 May 2000; pp. 96–99.
51. Huang, S.; Tang, L.; Hupy, J.P.; Wang, Y.; Shao, G. A commentary review on the use of normalized difference vegetation index (NDVI) in the era of popular remote sensing. *J. For. Res.* **2021**, *32*, 1–6. [CrossRef]
52. Miao, C.; Yu, S.; Hu, Y.; Zhang, H.; He, X.; Chen, W. Review of methods used to estimate the sky view factor in urban street canyons. *Build. Environ.* **2020**, *168*, 106497. [CrossRef]
53. Yang, J.; Yang, Y.; Sun, D.; Jin, C.; Xiao, X. Influence of urban morphological characteristics on thermal environment. *Sustain. Cities Soc.* **2021**, *72*, 103045. [CrossRef]
54. Lan, Y.; Zhan, Q. How do urban buildings impact summer air temperature? The effects of building configurations in space and time. *Build. Environ.* **2017**, *125*, 88–98. [CrossRef]
55. Huang, F.; Jiang, S.; Zhan, W.; Bechtel, B.; Liu, Z.; Demuzere, M.; Huang, Y.; Xu, Y.; Ma, L.; Xia, W.; et al. Mapping local climate zones for cities: A large review. *Remote Sens. Environ.* **2023**, *292*, 113573. [CrossRef]
56. Houet, T.; Pigeon, G. Mapping urban climate zones and quantifying climate behaviors—An application on Toulouse urban area (France). *Environ. Pollut.* **2011**, *159*, 2180–2192. [CrossRef]
57. Thomas, L.; Grimmond, C.S.B. Characterization of Energy Flux Partitioning in Urban Environments: Links with Surface Seasonal Properties. *J. Appl. Meteorol. Clim.* **2012**, *51*, 219–241.
58. Rodler, A.; Leduc, T. Local climate zone approach on local and micro scales: Dividing the urban open space. *Urban Clim.* **2019**, *28*, 100457. [CrossRef]
59. Zheng, Z.; Luo, F.; Li, N.; Gao, H.; Yang, Y. Impact of Local Climate Zones on the Urban Heat and Dry Islands in Beijing: Spatial Heterogeneity and Relative Contributions. *J. Meteorol. Res.* **2024**, *38*, 126–137. [CrossRef]
60. Li, X.; Yeh, A.G. Neural-network-based cellular automata for simulating multiple land use changes using GIS. *Int. J. Geogr. Inf. Sci.* **2002**, *16*, 323–343. [CrossRef]
61. Tang, B.H.; Zhan, C.; Li, Z.L.; Wu, H.; Tang, R. Estimation of Land Surface Temperature from MODIS Data for the Atmosphere with Air Temperature Inversion Profile. *IEEE J. Sel. Top. Appl. Earth Obs. Remote Sens.* **2017**, *10*, 2976–2983. [CrossRef]

62. Rongali, G.; Keshari, A.K.; Gosain, A.K.; Khosa, R. A Mono-Window Algorithm for Land Surface Temperature Estimation from Landsat 8 Thermal Infrared Sensor Data: A Case Study of the Beas River Basin, India. *Pertanika J. Sci. Technol.* **2018**, *26*, 829–840.
63. Song, T.; Duan, Z.; Liu, J.; Shi, J.; Yan, F.; Sheng, S. Comparison of four algorithms to retrieve land surface temperature using Landsat 8 satellite. *Natl. Remote Sens. Bull.* **2015**, *19*, 451–464.
64. Elith, J.; Leathwick, J.R.; Hastie, T. A working guide to boosted regression trees. *J. Anim. Ecol.* **2008**, *77*, 802–813. [CrossRef]
65. Hair, J.F.; Black, W.C.; Babin, B.J.; Anderdon, R.E. *Multivariate Data Analysis*, 7th ed.; Prentice Hall: Upper Saddle River, NJ, USA, 2009.
66. Wang, R.; Cai, M.; Ren, C.; Bechtel, B.; Xu, Y.; Ng, E. Detecting multi-temporal land cover change and land surface temperature in Pearl River Delta by adopting local climate zone. *Urban Clim.* **2019**, *28*, 100455. [CrossRef]
67. Guo, G.; Zhou, X.; Wu, Z.; Xiao, R.; Chen, Y. Characterizing the impact of urban morphology heterogeneity on land surface temperature in Guangzhou, China. *Environ. Model. Softw.* **2016**, *84*, 427–439. [CrossRef]
68. United Nations Department of Economic and Social Affairs. *68% of the World Population Projected to Live in Urban Areas by 2050, Says UN.*; Revision of World Urbanization Prospects; United Nations: New York, NY, USA, 2018.
69. Gong, Y.; Li, X.; Liu, H.; Li, Y. The Spatial Pattern and Mechanism of Thermal Environment in Urban Blocks from the Perspective of Green Space Fractal. *Buildings* **2023**, *13*, 574. [CrossRef]
70. Naeem, S.; Naeem, S.; Naeem, S.; Cao, C.; Qazi, W.A.; Zamani, M.; Wei, C.; Acharya, B.K.; Rehman, A.U. Studying the Association between Green Space Characteristics and Land Surface Temperature for Sustainable Urban Environments: An Analysis of Beijing and Islamabad. *ISPRS Int. J. Geo-Inf.* **2018**, *7*, 38. [CrossRef]
71. Turhan, C.; Özbey, M.F.; Lotfi, B.; Gökçen Akkurt, G. Integration of psychological parameters into a thermal sensation prediction model for intelligent control of the HVAC systems. *Energy Build.* **2023**, *296*, 113404. [CrossRef]

Disclaimer/Publisher's Note: The statements, opinions and data contained in all publications are solely those of the individual author(s) and contributor(s) and not of MDPI and/or the editor(s). MDPI and/or the editor(s) disclaim responsibility for any injury to people or property resulting from any ideas, methods, instructions or products referred to in the content.